Acta Pharmaceutica Sinica B 2026;16(4):2375−2395

Chinese Pharmaceutical Association
Institute of Materia Medica, Chinese Academy of Medical Sciences

Acta Pharmaceutica Sinica B

www.elsevier.com/locate/apsb
www.sciencedirect.com

ORIGINAL ARTICLE

FTO-mediated m^{6}A depletion drives prenatal prednisone exposure-induced cortical neurogenesis deficits and long-term anxiety-depression-like behaviors in offspring

Cuiping Qi[a,†], Juanjuan Guo[a,†], Sen Zhu[a,†], Keshu Liu[b], Yifan Liu[c], Mingcui Luo[a], Xiuping Jin[a], Gaole Dai[a], Pu Yang[d], Shouyi Wang[d], Xiong Chen[b], Huijun Chen[a], Hui Wang[e,f], Dan Xu[a,f,g,*]

[a]*Department of Obstetric, Zhongnan Hospital of Wuhan University, School of Pharmaceutical Sciences, Wuhan University, Wuhan 430071, China*
[b]*Department of Otorhinolaryngology-Head and Neck Surgery, Zhongnan Hospital of Wuhan University, Wuhan 430071, China*
[c]*Department of Pediatric Surgery, Zhongnan Hospital of Wuhan University, Wuhan 430071, China*
[d]*Department of Pediatrics, Zhongnan Hospital of Wuhan University, Wuhan 430071, China*
[e]*Department of Pharmacology, Taikang Medical School (School of Basic Medical Sciences), Wuhan University, Wuhan 430071, China*
[f]*Hubei Provincial Key Laboratory of Developmentally Originated Disease, Wuhan 430071, China*
[g]*Ministry of Education Key Laboratory of Combinatorial Biosynthesis and Drug Discovery, Wuhan 430071, China*

Received 21 April 2025; received in revised form 10 November 2025; accepted 19 January 2026

KEY WORDS

Prednisone;
N^6-methyladenosine modifications;
Radial glial cells;
Neurogenesis impairment;
Neuregulin-1;
Fat mass and obesity-

Abstract Prednisone is widely used to treat pregnancy-complicated autoimmune diseases, but the impact of prenatal prednisone exposure (PPE) on offspring neurodevelopment is unclear. Clinical follow-up using the Ages and Stages Questionnaires (ASQ:SE-2 and ASQ-3) revealed a strong association between PPE and neurodevelopmental abnormalities. In a rat model, PPE significantly inhibited the proliferation and differentiation of cortical radial glial cells (RGCs), impairing cortical neurogenesis and leading to anxiety- and depression-like behaviors. Mechanistically, PPE upregulated fat mass and obesity-associated protein (FTO) nuclear recruitment in RGCs, depleting N^6-methyladenosine (m^{6}A) modifications and stabilizing *Crebbp*/*Ep300* mRNA, which activated genes related to cell cycle arrest and

*Corresponding author.
E-mail address: xuyidan70188@whu.edu.cn (Dan Xu).
†These authors made equal contributions to this work.
Peer review under the responsibility of Chinese Pharmaceutical Association and Institute of Materia Medica, Chinese Academy of Medical Sciences.

https://doi.org/10.1016/j.apsb.2026.01.026
2211-3835 © 2026 The Authors. Published by Elsevier B.V. on behalf of Chinese Pharmaceutical Association and Institute of Materia Medica, Chinese Academy of Medical Sciences. This is an open access article under the CC BY-NC-ND license (http://creativecommons.org/licenses/by-nc-nd/4.0/).

associated protein;
Offspring;
Histone 3 at lysine 27 acetylation

neuronal differentiation *via* histone 3 at lysine 27 acetylation (H3K27ac) modifications. The key role of FTO in PPE-induced neurodevelopmental impairments was confirmed using *Ep3*00 shRNA, *Fto* overexpression lentivirus, and a conditional *Fto* knockout mouse model ($Fto^{fl/fl}$; Nestin-Cre). Notably, early postnatal neuregulin-1 supplementation promoted RGCs proliferation and alleviated behavioral abnormalities.

© 2026 The Authors. Published by Elsevier B.V. on behalf of Chinese Pharmaceutical Association and Institute of Materia Medica, Chinese Academy of Medical Sciences. This is an open access article under the CC BY-NC-ND license (http://creativecommons.org/licenses/by-nc-nd/4.0/).

1. Introduction

With advances in immunomodulatory therapies, the quality of life and life expectancy of patients with autoimmune diseases have significantly improved, enabling more women to fulfill their reproductive aspirations. However, the number of pregnancies complicated by autoimmune diseases has risen rapidly. A cross-sectional analysis of U.S. delivery hospitalizations from 2015 to 2020 showed that among 18,866,050 deliveries, 0.27% were complicated by autoimmune connective tissue diseases, with systemic lupus erythematosus at 0.134% and rheumatoid arthritis at 0.127%[1]. To control disease progression and ensure pregnancy safety, many of these patients require glucocorticoid therapy, such as prednisone (PDN), during pregnancy to suppress immune responses. PDN, one of the most commonly used oral glucocorticoids, is prescribed in 20%−60% of such cases[2]. Fetal growth restriction is often associated with adverse effects on the nervous system, such as an increased incidence of neurodevelopmental disorders—including cognitive impairment, autism spectrum disorders, and depression—in growth-restricted children[3-6]. However, research on the impact of PPE on neurodevelopment in offspring and its long-term neurobehavioral consequences remains limited, particularly with regard to the underlying molecular and cellular mechanisms.

The development of the central nervous system (CNS) is pivotal in establishing its functional maturation and stability[7]. Any defects in this process are closely linked to a heightened risk of severe psychiatric disorders, including depression, autism spectrum disorder, and schizophrenia[8-10]. Increasing epidemiological and clinical evidence underscores a profound connection between neurodevelopment and the onset of psychiatric conditions. For instance, data analyses from 2 major UK cohort studies revealed significant associations between key neurodevelopmental traits in childhood and depressive symptoms[11]. Similarly, a longitudinal twin study in Sweden highlighted the prevalence of neurodevelopmental impairments among adolescents at high risk for anxiety and depression[12]. A dynamic balance between neural stem cell proliferation and neurogenesis represents a core mechanism of neurodevelopment, and disruptions in this equilibrium are considered fundamental pathological bases for psychiatric disorders[13,14]. During mammalian cortical development, radial glial cells (RGCs) function as essential neural stem cells[15]. They self-renew and undergo precise differentiation to sequentially produce deep- and upper-layer cortical neurons, eventually transitioning into glial cells[16]. This highly orchestrated developmental process is driven by a complex network of genetic regulatory mechanisms[17]. Recent studies have highlighted the importance of epigenetic modifications, particularly N^6-methyladenosine (m^6A) RNA methylation, in regulating these processes. m^6A is the most abundant RNA methylation modification, accounting for approximately 80% of RNA base methylation, and is highly enriched in the mammalian brain[18,19]. Evidence suggests that m^6A modifications regulate gene expression by modulating RNA stability, translation efficiency, and post-transcriptional processing, thereby influencing neural stem cell differentiation, embryonic stem cell self-renewal, and the formation of neuronal networks[20,21]. These findings position m^6A modification as a focal point in studying neurodevelopment and its disorders, highlighting its significant potential in regulating embryonic neural stem cell development.

Given the widespread use of PDN during pregnancy and its potential neurotoxicity, this study aims to investigate the impact of PPE on offspring neurodevelopment. Through follow-up assessments using the Ages and Stages Questionnaires: Social-Emotional, Second Edition (ASQ:SE-2) and the Ages and Stages Questionnaires, Third Edition (ASQ-3) in infants and toddlers aged 6 to 24 months, we identified a significant association between PPE and neurodevelopmental abnormalities. To further elucidate its molecular mechanisms, we employed methylated RNA immunoprecipitation sequencing (MeRIP-seq) analysis of the cortex from PPE offspring rats, *in vitro* culture of RGC, and the fat mass and obesity-associated protein conditional knockout (cKO) mouse model ($Fto^{f/fl}$; Nestin-Cre), revealing that PPE regulates RGC cell cycle and neuronal differentiation genes *via* the *Fto*-cAMP response element-binding protein binding protein (*Crebbp*)/E1A binding protein p300 (*Ep300*)-histone 3 at lysine 27 acetylation (H3K27ac) pathway. Specifically, PPE limited the proliferation and differentiation of RGCs, leading to cortical neurogenesis disruption, which manifested as anxiety- and depression-like behaviors in adulthood. Early postnatal supplementation with neuregulin-1 (NRG-1) significantly promoted the proliferation of RGCs in PPE offspring, partially restored cortical neurogenesis, and effectively alleviated anxiety- and depression-like behaviors in adulthood. This study not only provides new insights into the impact of PPE on offspring neurodevelopment but also offers a theoretical foundation and experimental evidence for developing early interventions and therapeutic strategies for anxiety and depression.

2. Materials and methods

2.1. Human subjects and follow-up

This study protocol was approved by the Medical Ethics Committee of Zhongnan Hospital, Wuhan University (Approval No. [2023141K]), to investigate the impact of PPE on offspring neurodevelopment. A cross-sectional survey was conducted involving pregnant women who delivered at Zhongnan Hospital, Wuhan University, between July 2021 and July 2024, along with their

infants and toddlers. Inclusion criteria comprised full-term pregnant women diagnosed with autoimmune diseases during pregnancy and their matched controls without autoimmune diseases. The autoimmune conditions involved include systemic lupus erythematosus, antiphospholipid syndrome, Sjögren's syndrome, and undifferentiated connective tissue disease, as summarized in Supporting Information Table S1. Exclusion criteria included twin pregnancies, neonatal asphyxia, birth defects or malformations, and maternal psychiatric or infectious diseases (*e.g.*, HIV, hepatitis, syphilis). By July 2024, a total of 340 infants and toddlers were enrolled and classified into 3 groups based on maternal autoimmune disease status and prednisone use: Control, the autoimmune disease PPE group, and the autoimmune disease prenatal prednisone non-exposed (PPNE) group. Participants were further stratified into age groups of 6, 12, 18, and 24 months. At the start of the study, all parents were thoroughly informed about the research objectives and provided written informed consent. Physical assessments, including height and weight measurements, were conducted by professional pediatricians.

Neurodevelopment was assessed using 2 parent-reported questionnaires: ASQ:SE-2 and ASQ-3. ASQ:SE-2 measures 7 domains of social-emotional development, including self-regulation, compliance, communication, adaptive functioning, autonomy, affect, and interpersonal interaction. ASQ-3 assesses 5 areas of developmental milestones: communication, gross motor, fine motor, problem-solving, and personal-social skills. Both questionnaires were completed through telephone interviews or online submissions by parents, with professional evaluators recording and scoring the results based on the responses.

ASQ:SE-2 scores were categorized as "below the cutoff" or "at or above the cutoff" based on questionnaire standards. Scores "at or above the cutoff" indicated potential social-emotional behavior abnormalities requiring further intervention and monitoring. ASQ-3 scores were divided into "normal", "monitoring required", and "abnormal" categories, with "below the cutoff" classified as developmental delay, recommending clinical follow-up or referral to early intervention services.

Detailed baseline data were collected from both mothers and offspring. Maternal data included age, gravidity, mode of delivery, pregnancy complications (*e.g.*, gestational hypertension, gestational diabetes, hypothyroidism), and medication use. Offspring data encompassed gestational age, birth weight, current height and weight, feeding practices, types of nutritional supplements, genetic screening results, recent medications, and illnesses. Finally, the ASQ:SE-2 and ASQ-3 scores of infants and toddlers aged 6 to 24 months were systematically analyzed to evaluate the potential impact of PPE on offspring neurodevelopment.

2.2. Animal subjects and treatments

All experimental protocols involving rats were approved by the Institutional Animal Care and Use Committee (IACUC) of Wuhan University Animal Experimentation Center (IACUC No. WP20210060). Animal care and use were conducted in strict accordance with the guidelines established by the Chinese Animal Welfare Committee.

Specific pathogen-free (SPF) Wistar rats (females: 240 g; males: 350 g; 9−10 weeks old) were obtained from SPF Biotechnology Co., Ltd. (Beijing, China). Before the experiments, they were acclimated for 1 week under standard conditions. Mating was confirmed by the presence of sperm in vaginal smears the next morning, marking GD0. Pregnant rats were then randomly divided into the control and PPE groups. To simulate clinical practice, low-dose prednisolone (2.5−10 mg/day) is recommended during pregnancy for autoimmune disease management[22]. Based on the human-to-rat dose conversion ratio (1:6.17)[23,24], pregnant rats in the PPE group were administered 0.25 mg/kg/day prednisolone *via* oral gavage from GD0 to GD20. Control rats received an equivalent volume of vehicle (0.5% CMC-Na, 5 mL/kg/day) by gavage. On GD17 and GD20, pregnant rats were sacrificed after overnight fasting to collect fetal samples *via* cesarean section. Fetal cortices were harvested after sex identification. Remaining pregnant rats were maintained until delivery, with 10−14 pups per litter considered eligible for study ($n = 12$ per group). The day of delivery was designated as PD0. Offspring were sexed and weighed, with 1 male pup per litter randomly selected for sacrifice at PD3 and PD10 to collect cortical tissues. The remaining offspring were reared to adulthood (PW12) for behavioral testing ($n = 8$ per group), after which they were sacrificed, and cortical tissues were collected for morphological and molecular analyses.

NRG-1 animal interventions. From each litter in the control and PPE groups ($n = 12$ per group), 6 male offspring were randomly assigned to receive a 7-day intervention with NRG-1 (PeproTech, Cranbury, NJ, USA). The study included 4 groups: Control_S, PPE_S, PPE_N, and Control_N. NRG-1 (10 μg/kg/day) or an equivalent volume of saline was administered intraperitoneally[25]. On PD3 and PD10, 1 male pup from each group was randomly sacrificed to collect cortical tissues. Remaining offspring were reared to PW12 for behavioral testing ($n = 8$ per group), followed by euthanasia and cortical tissue collection for morphological and molecular analyses.

C57BL/6J, *Fto*$^{f/f}$; Nestin-Cre mice were obtained from Cyagen Biotechnology Co., Ltd. (Suzhou, China). *Fto* cKO mice were generated using CRISPR-Cas9 gene-editing technology, employing Cas9 protein and gRNAs (gRNA-A1: ACAG TTAAGATCACTCCCGC-CGG; gRNA-B1: TCTGGGCTT CAGTGTCTGGC-TGG) targeting intron 1 and intron 2 of the mouse Exoc4 gene with donor vectors containing loxP sites. Fertilized embryos were implanted into surrogate female mice, and GD0 was designated as the first day post-implantation. Pregnant mice were housed under a 12 h light/dark cycle at 23 ± 2 °C in the Wuhan University Animal Experimentation Center, with experimental protocols approved by the IACUC (Approval No. WP20240139). Pregnant mice were randomly assigned to the control or PPE group. Based on the human-to-mouse dose conversion ratio (1:12.3) [23,24], pregnant mice in the PPE group received 0.5 mg/kg/day prednisolone *via* gavage from GD0 to GD18, while the control group received an equal volume of solvent (0.5% CMC-Na, 5 mL/kg/day). On GD18, pregnant mice were fasted overnight and sacrificed to collect fetal samples *via* cesarean section. Fetal cortices were harvested following sex identification.

2.3. Behavioral testing

Open field test (OFT). The test rats were placed in an opaque acrylic box with an open top (100 cm × 100 cm × 20 cm) and allowed to freely explore the environment. The movement trajectories of each rat were recorded over a 5-min session, with the apparatus cleaned using 75% ethanol between tests to prevent olfactory interference. Finally, analysis was performed using the Smart v3.0 video tracking system (Panlab, Cornellà, Spain).

Novelty suppressed feeding test (NSFT). Before the experiment, the apparatus was cleaned with 75% ethanol. Each rat was placed in an open-top opaque acrylic box (100 cm × 100 cm × 20 cm), with a novel food container positioned at the center of the field. Feeding latency was measured from entry into the new environment to the first feeding event. The 5-min test was recorded and analyzed using the Smart v3.0 video tracking system.

Elevated plus maze (EPM). The EPM featured 2 open and 2 enclosed arms (50 cm × 10 cm × 40 cm) extending from a central platform (10 cm × 10 cm). After ethanol (75%) cleaning to eliminate odor cues, rats were positioned on the platform for a 5-min exploration. Behavioral parameters, including arm preference and movement patterns, were quantified using the Smart v3.0 system.

Forced swimming test (FST). The test rats were placed in a cylindrical acrylic tank with warm water to a depth of 15 cm to minimize additional stress caused by cold. Each rat swam for 5 min, during which immobility was defined as the absence of active movements while maintaining the head above the water. Swimming and immobility times were recorded and analyzed using the Smart v3.0 tracking system.

Sucrose preference test (SPT). Rats underwent 48-h sucrose training, beginning with dual 1% sucrose bottles for 24 h, followed by 1 sucrose bottle and 1 water bottle with position rotation every 12 h. After 24-h food and water restriction, sucrose preference was assessed by measuring 24-h consumption from 2 bottles (1% sucrose vs. water), with positions alternated at 12-h intervals to control for side preference.

Novel object recognition test (NORT). In the experiment, rats were introduced to a known setting featuring 2 unfamiliar items and given 5 min to investigate. Following a 24-h interval, one of the original items was substituted with a new object during the test phase, and the rats were reintroduced to the setting for another 5-min exploration period. The Smart v3.0 video tracking system was utilized to document movement paths and behavioral metrics. The cognitive index was calculated as Eq. (1):

$$\begin{aligned}\text{Cognitive index} = &(\text{Time exploring the new object}\\ &-\text{Time with the familiar object})\\ &/\text{Total exploration time}\end{aligned} \quad (1)$$

2.4. Isolation and culture of primary RGCs

RGCs were extracted from GD14 Wistar rat embryos. After euthanizing the pregnant rat, embryos (7−8 per extraction) were collected under sterile conditions, and cortical tissues were excised and finely minced. The tissue fragments were digested with collagenase IV (Gibco, Carlsbad, CA, USA) at 37 °C for 30 min. Digestion was terminated using fetal bovine serum, followed by filtration through a sterile 200-mesh nylon sieve to obtain a single-cell suspension. The suspension was centrifuged, the supernatant discarded, and the cells resuspended in neural stem cell culture medium (composition: 97 mL DMEM/F12 basal medium, 20 ng/mL EGF, 20 ng/mL bFGF, 2 mL B-27, and 1 mL 100 × PS). The RGCs were seeded into cell culture flasks and incubated at 37 °C in a 5% CO_2 atmosphere. After approximately 5 days, neurospheres were observed. These were dissociated into single cells using Accutase cell dissociation enzyme (Gibco) and subjected to 3 rounds of purification by passaging. The purified cells were resuspended in the neural stem cell culture medium, counted, and assessed for viability. Subsequently, cells were seeded at a density of 1.5×10^4 cells/mL into poly-L-lysine-precoated plates to allow adhesion. The culture was maintained in neural stem cell culture medium for subsequent experimental assays.

Induction of differentiation of primary RGCs. Following dissociation into single cells using Accutase, RGCs were resuspended in differentiation medium (composition: 97 mL DMEM/F12 basal medium, 2 mL FBS, and 1 mL 100 × PS) and seeded into six-well plates. The cultures were prepared for subsequent experimental analysis.

Lentiviral intervention. Lentiviral constructs for *Fto* overexpression (Fto^{oe}) and *Ep300* knockdown (shRNA sequence: ATGACTTACCAGATGAATTAA) were obtained from General Biol (Chuzhou, China). RGCs were prepared as a single-cell suspension at a density of 1.5×10^4 cells/mL and seeded into plates. The lentiviral constructs were diluted in neural stem cell culture medium to various multiplicity of infection (MOI = 10, 20, 50, 80, 100) and incubated with RGCs in the presence of puromycin (8 μg/mL) at 37 °C for 24 h. The medium was then replaced with fresh neural stem cell culture medium, and fluorescence intensity was observed at 48- and 72-h post-transfection to determine optimal infection conditions. Both Fto^{oe} and *Ep300* shRNA knockdown were achieved under conditions of MOI = 20 for 72 h. The resultant Fto^{oe} and *Ep300* knockdown cell lines were used for subsequent experimental assays.

2.5. MeRIP-seq analysis

Total RNA was isolated using Trizol reagent, with quality assessed by Nanodrop ND-1000 and Bioanalyzer 2100 (concentration >50 ng/μL, RIN >7.0, $OD_{260/280}$ >1.8). Poly(A)$^+$ RNA was purified using Dynabeads Oligo(dT), fragmented, and subjected to m^6A immunoprecipitation with specific antibody (Synaptic Systems, Göttingen, Germany, 202003). Library preparation included cDNA conversion, end repair, A-tailing, adapter ligation, size selection (180−220 bp), and UDG treatment, followed by PE150 sequencing on Illumina Novaseq 6000. Bioinformatics analysis involved HISAT2 alignment to reference genome v104, exomePeak-based peak calling, ANNOVAR annotation, and HOMER motif analysis. Transcript quantification (FPKM) and assembly were performed using StringTie, with differential expression analysis (edgeR) applying thresholds of $|FC| \geq 2$ and $P < 0.05$.

2.6. RT-qPCR analysis

Total RNA extraction from rat cortical tissues and primary RGCs was performed using Trizol reagent according to the manufacturer's instructions. Subsequent cDNA synthesis was carried out with Hiscript III RT SuperMix for qPCR (+gDNA wiper) (Vazyme, Nanjing, China), followed by quantitative PCR analysis using Taq Pro Universal SYBR qPCR Master Mix on a QuantStudio 5 platform. Gene expression quantification was normalized to *Gapdh* and calculated *via* the $2^{-\Delta\Delta Ct}$ method, with corresponding primer sequences detailed in Supporting Information Table S2.

2.7. ChIP-qPCR assay

ChIP-qPCR assays were conducted as previously described[26]. Cortical tissues were cross-linked with 1% formaldehyde at room

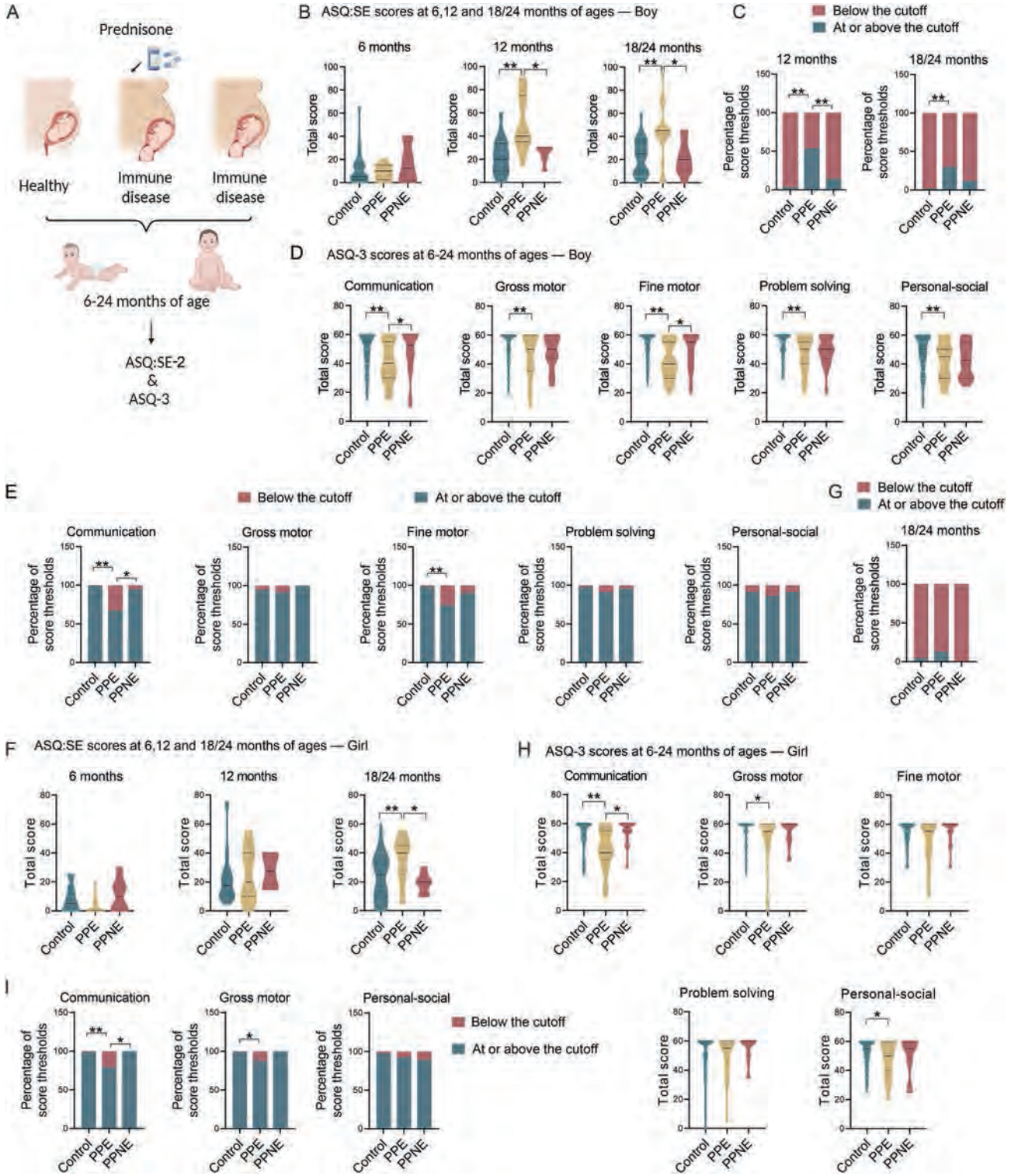

Figure 1 Ages and Stages Questionnaires: Social-Emotional, Second Edition (ASQ:SE-2) and Ages & Stages Questionnaire, Third Edition (ASQ-3) assessments and abnormality rates in infants aged 6 to 24 months from control, prenatal prednisone-exposed (PPE), and prenatal prednisone non-exposed (PPNE) groups. (A) Study design for ASQ:SE-2 and ASQ-3 assessments. (B), (F) Total raw ASQ:SE-2 scores at 6, 12, and 18/24 months in male and female infants. (C), (G) Percentages of abnormal ASQ:SE-2 scores at 12 and 18/24 months in male and female infants. (D), (H) Raw scores across 5 ASQ-3 subdomains—communication, gross motor, fine motor, problem-solving, and personal-social male and female infants aged 6 to 24 months. (E), (I) Percentages of abnormal ASQ-3 scores in male and female infants aged 6 to 24 months. Data are presented as mean ± SEM; $*P < 0.05$, $**P < 0.01$ *vs.* respective Control or PPNE.

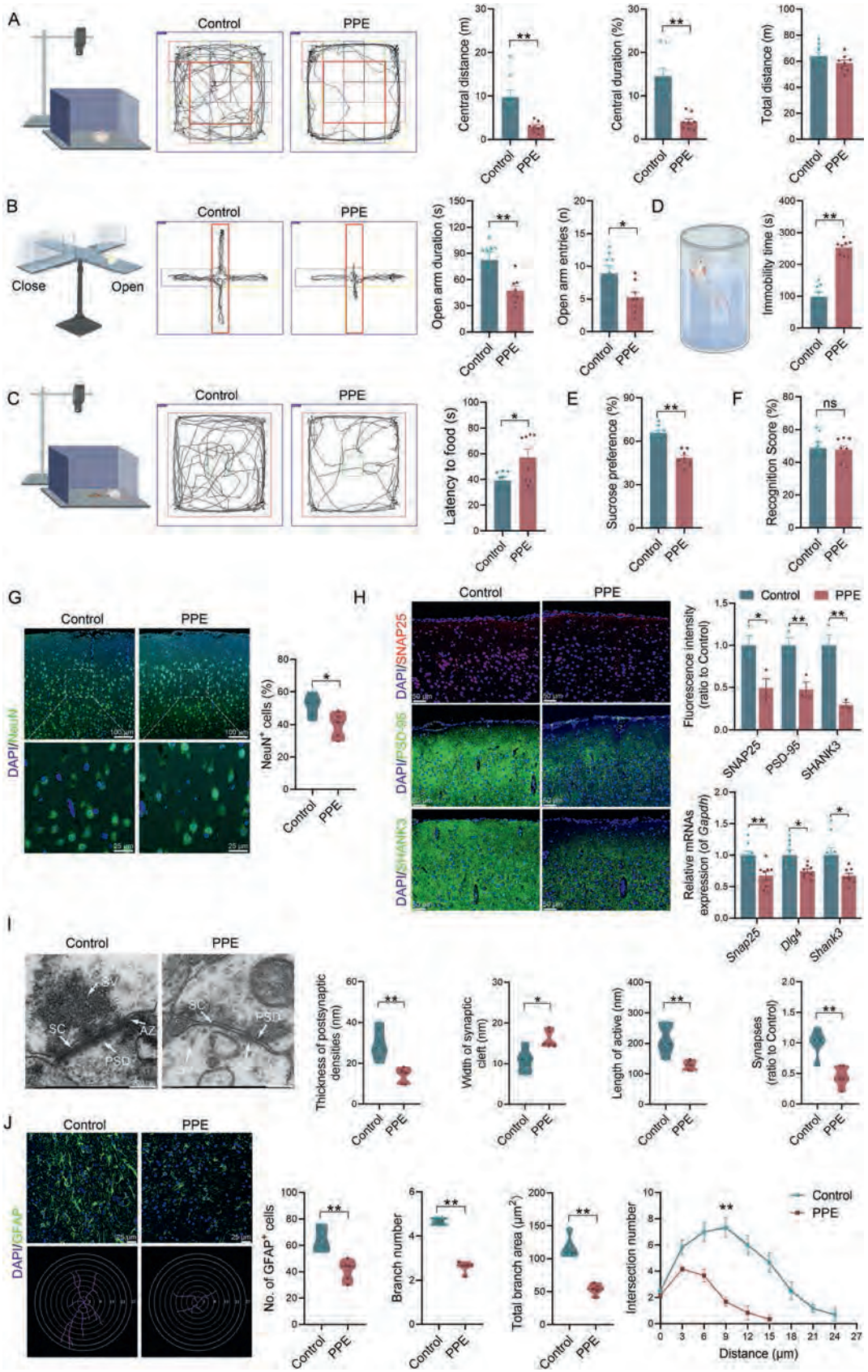

Figure 2 PPE induced anxiety- and depression-like behaviors in postnatal week 12 (PW12) adult offspring rats, accompanied by cortical nerve cells reduction and structural abnormalities. (A) Representative track plots from the open field test (OFT) and quantification of distance traveled in the center zone, time spent in the center zone, and total distance traveled, $n = 8$. (B) Representative track plots from the elevated plus maze

temperature, centrifuged, and homogenized in PBS containing 1% protease inhibitor cocktail. Chromatin was fragmented by sonication. Pre-treated Protein G agarose beads were incubated overnight with antibodies targeting H3K9ac (ABclonal, Wuhan, China, A7255), H3K14ac (ABclonal, A7254), and H3K27ac (ABclonal, A7253), along with chromatin. After washing the immunoprecipitated complexes, DNA-chromatin cross-links were reversed. DNA was purified using a DNA purification kit (Tiangen, Beijing, China, Cat. #DP204-03) and analyzed by RT-qPCR with gene-specific primers.

2.8. Hematoxylin−eosin (HE) staining and analysis

Cortical tissues from offspring rats were fixed overnight in 4% paraformaldehyde. Following fixation, the tissues underwent dehydration, clearing, and paraffin embedding to prepare coronal brain sections, which were cut to a thickness of 3−5 μm. Sections were stained using an HE staining kit as per the manufacturer's protocol and mounted with neutral balsam. Histological analysis and imaging were performed using a conventional optical microscope (Nikon, Tokyo, Japan). Cortical thickness was measured by analyzing the stained images with ImageJ software (version 6.0, Media Cybernetics Inc., Rockville, MD, USA).

2.9. Immunofluorescence staining and analysis

Immunofluorescence staining was performed on deparaffinized and cryosections after antigen retrieval in citrate buffer (pH 6.0). Sections were permeabilized (0.25% Triton X-100 in PBS, 30 min), blocked (10% goat serum in PBST), and incubated with primary antibodies (1:200 unless specified): Rabbit anti-SATB2 (1:200, Abcam, ab92446), Rabbit anti-TBR1 (1:200, Abcam, ab183032), Rabbit anti-CTIP2 (1:200, ABclonal, A21767), Rabbit anti-CUX1 (1:200, ABclonal, A2213), Rabbit anti-PAX6 (1:200, Abcam, ab195045), Rabbit anti-BrdU(1:200, ABclonal, A1482), Rabbit anti-NeuN (1:200, ABclonal, A19086), Rabbit anti-GFAP(1:400, Abcam, Cambridge, UK, ab68428), Rabbit anti-MAP2 (1:1000, NBP3-05552, Novus Biologicals, Centennial, CO, USA). For BrdU detection, sections underwent HCl treatment (1 mol/L, 37 °C, 30 min) followed by borate buffer neutralization. Secondary staining used ABflo 594/488-conjugated Goat Anti-Rabbit IgG (1:200, ABclonal, AS039/AS073), with DAPI counterstaining. Imaging was performed using a Leica SP8 confocal microscope and analyzed with ImageJ.

2.10. TEM analysis

Cortical tissues were dissected into 1 mm^3 cubes and sequentially fixed in 2.5% glutaraldehyde followed by 1% osmium tetroxide. Following phosphate buffer (0.1 mol/L) rinses, samples underwent ethanol gradient dehydration, embedding, and sectioning. Ultrathin sections were double-stained with uranyl acetate (3%) and lead citrate, then examined using a Hitachi transmission electron microscope (Hitachi, Tokyo, Japan). Morphological analysis was performed using ImageJ software.

2.11. Protein extraction and Western blot analysis

Total protein was isolated from fetal cortical tissues using radioimmunoprecipitation assay lysis buffer, with concentrations determined by bicinchoninic acid assay. Nuclear and cytoplasmic fractions were separated using a commercial extraction kit (Applygen, Beijing, China, P1200). Equal amounts of protein (adjusted to uniform concentration) were denatured in loading buffer at 100 °C for 10 min. Following SDS−PAGE separation, proteins were transferred to PVDF membranes and probed with specific primary antibodies: H3 (1:2000, ABclonal, A2348), H3K14ac (1:1000, ABclonal, A7254), H3K9ac (1:1000, ABclonal, A7255), H3K27ac (1:1000, ABclonal, A7253), FTO (1:2000, Proteintech, Rosemont, IL, USA, 27226-1-AP), EP300 (1:500, Abcam, ab14984), and CREBBP (1:1000, Santa Cruz, Dallas, TX, USA, SC-365387). Membranes were then incubated with HRP-conjugated secondary antibodies (1:10,000, ABclonal, AS003/AC206) and visualized using chemiluminescence (Bridgen, Beijing, China, BR10273). Band intensities were quantified by grayscale analysis.

2.12. Dot blot assay

RNA was extracted from primary RGC or GD17 fetal cortical tissues using the Dynabeads mRNA Purification Kit (Ambion, Austin, TX, USA, 61011). Each sample was analyzed in triplicate at three different concentrations, with 2 μL spotted per replicate. The purified RNA was pipetted onto a nylon membrane and allowed to dry completely. RNA was UV-crosslinked (Stratalinker 2400, 2 × auto program) and membranes were blocked (5% non-fat milk in PBST, 2 h). After overnight incubation with anti-m^6A antibody (1:2000, Abcam, A19841) at 4 °C, membranes were probed with HRP-conjugated secondary antibody (1:10,000, 2 h). Chemiluminescent detection was performed, with images acquired using Image-Pro Plus 6.0. RNA loading was verified by methylene blue staining (0.02% in 0.3 mol/L sodium acetate, pH 5.2), and m^6A levels were normalized accordingly.

2.13. Cell cycle analysis

Primary RGC cell cycle progression was assessed as previously outlined[27], adhering to the manufacturer's guidelines. Briefly, primary rat RGCs were treated with 10 μmol/L EdU (ABclonal, RM02832) for 2 h and rinsed with RGC culture medium. At

(EPM) and quantification of time spent in the open arms and number of entries into the open arms, $n = 8$. (C) Representative track plots from the novelty-suppressed feeding test (NSFT) and quantification of latency to feed, $n = 8$. (D) Immobility time in the forced swim test (FST), $n = 8$. (E) Sucrose consumption in the sucrose preference test (SPT), $n = 8$. (F) Discrimination index in the novel object recognition test (NORT), $n = 8$. (G) Representative images and quantification of neuronal nuclei (NeuN)-positive mature neurons in the cortex. Scale bar = 100 μm; white boxed regions are magnified. Scale bar = 25 μm, $n = 5$. (H) Representative immunofluorescence images and quantification of SNAP25, PSD-95, and SHANK3. Scale bar = 50 μm, $n = 3$. mRNA expression levels of *Snap25*, *Dlg4* and *Shank3*, $n = 8$. (I) Electron micrographs of neuronal synapses and quantification of postsynaptic density (PSD) thickness, synaptic cleft (SC) width, active zone (AZ) length, and synapse vesicle (SV) density per field of view. Scale bar = 200 nm, $n = 5$. (J) Representative images of glial fibrillary acidic protein (GFAP)-positive astrocytes and Sholl analysis, along with quantification of astrocyte count, branch length, volume, and branch number. Scale bar = 25 μm, $n = 5$. Data are presented as mean ± SEM; ns, no significance; $^*P < 0.05$, $^{**}P < 0.01$ *vs.* respective Control.

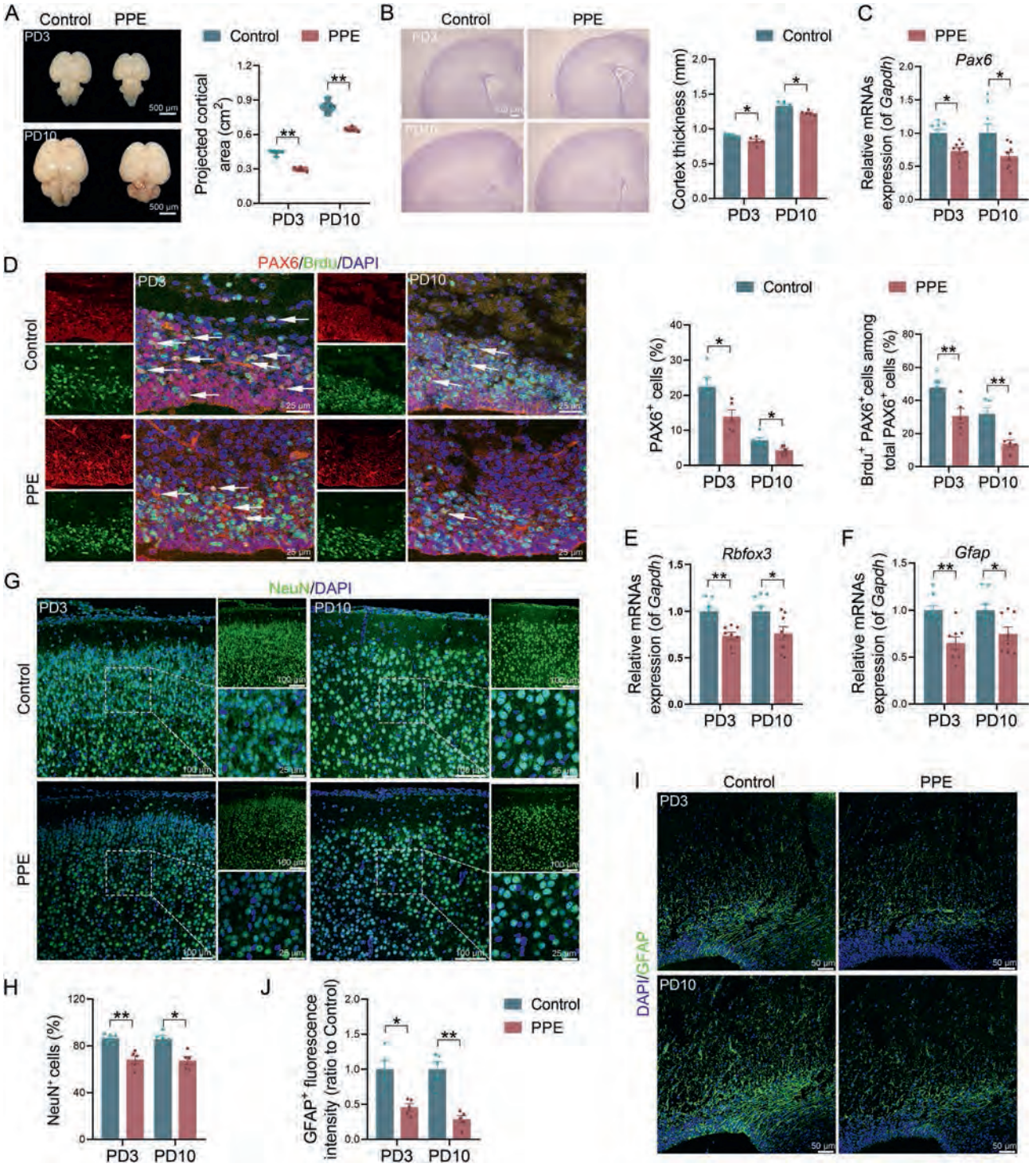

Figure 3 PPE induced cortical neurogenesis deficits in neonatal offspring at postnatal day 3 (PD3) and PD10. (A) Whole-brain images and quantification of cortical area. White dashed lines indicate the cortical area of one hemisphere. Scale bar = 500 μm, $n = 5$. (B) Hematoxylin-eosin (HE) stained images and quantification of cortical thickness. Scale bar = 500 μm, $n = 5$. (C) mRNA expression levels of paired box gene 6 (*Pax6*), $n = 8$. (D) Representative images of 5-bromodeoxyuridine (BrdU)/PAX6 double-positive cells and quantification. Scale bar = 25 μm, $n = 5$. mRNA expression levels of *Rbfox3* (E) and *Gfap* (F), $n = 8$. Representative images and quantification of NeuN-positive (G), (H) and GFAP-positive (I), (J) cells. Scale bar = 100 μm/50 μm; white boxes denote magnified regions. Scale bar = 25 μm, $n = 5$. Data are presented as mean ± SEM; $^{*}P < 0.05$, $^{**}P < 0.01$ *vs.* respective Control.

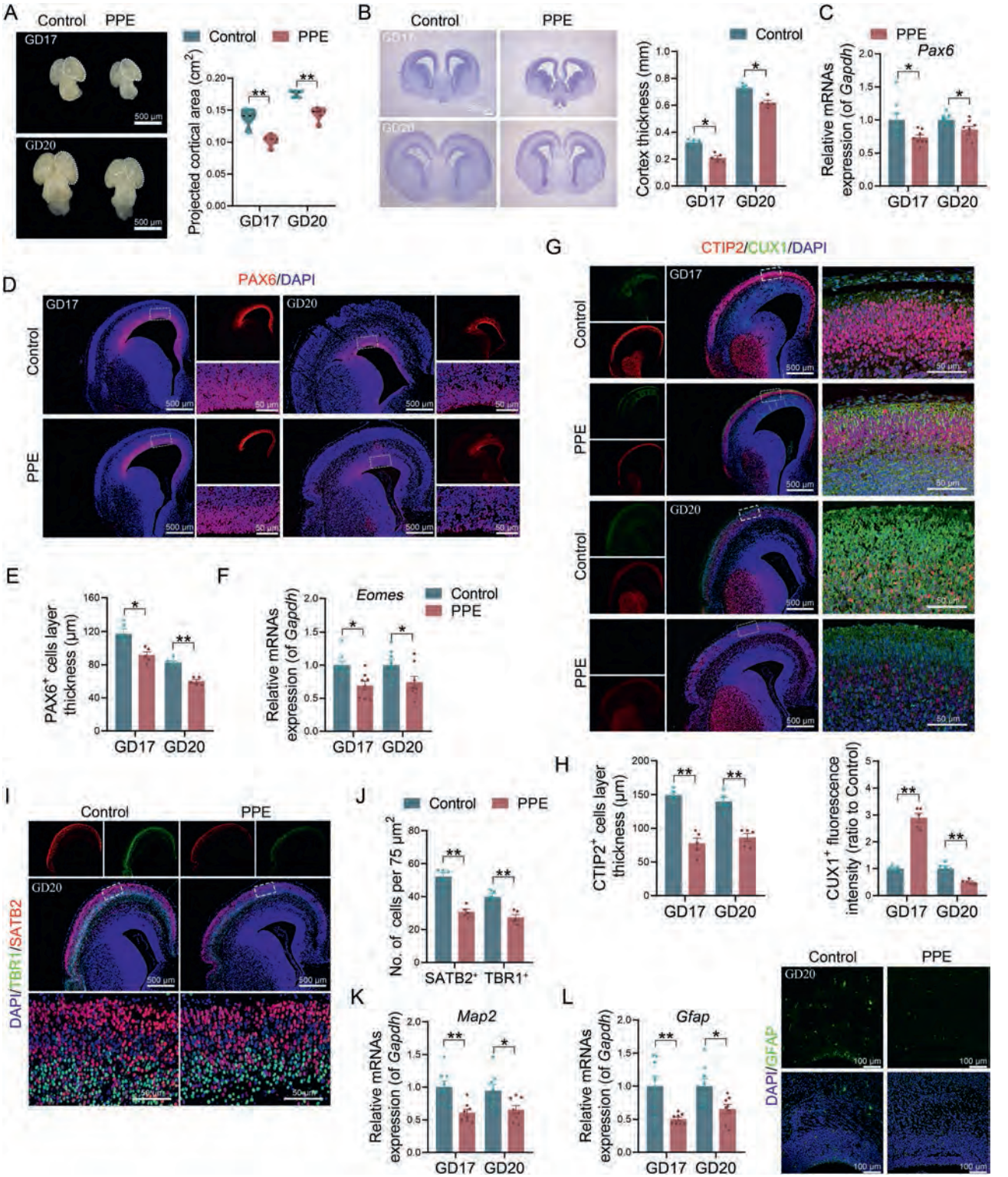

Figure 4 PPE inhibited the proliferation and differentiation of radial glial cells (RGCs) in the cortex of gestational day 17 (GD17) and GD20 fetal rats. (A) Whole-brain images and quantitative analysis of cortical area, with white dashed lines outlining the cortical area of a hemisphere. Scale bar = 500 μm, $n = 5$. (B) HE-stained images and quantification of cortical thickness. Scale bar = 500 μm, $n = 5$. (C) mRNA expression levels of *Pax6*, $n = 8$. (D) Immunofluorescence staining for PAX6 and quantitative analysis (E). Scale bar = 500 μm; white dashed rectangles indicate magnified regions. Scale bar = 50 μm, $n = 5$. (F) mRNA expression levels of *Eomes*, $n = 8$. (G) Immunofluorescence images for CUTL1-interacting protein 2 (CTIP2, red, deep-layer neuronal marker) and Cut-like homeobox 1 (CUX1, green, upper-layer neuronal marker), and quantitative analysis (H). Scale bar = 500 μm; white dashed rectangles indicate magnified regions. Scale bar = 50 μm, $n = 5$. (I), (J) Immunofluorescence images for special AT-rich sequence binding protein 2 (SATB2, red, upper-layer neuronal marker) and T-box brain protein 1

specified intervals, cells were dissociated using Accutase, fixed with 4% paraformaldehyde in PBS for 20 min at room temperature, and stained using the Click-iT Plus EdU Alexa Fluor 647 Flow Cytometry Assay Kit (ThermoFisher, Waltham, MA, USA, C10634). DNA was counterstained with DAPI, and flow cytometry was conducted on a BD LSRFortessa X-20 flow cytometer (BD Bioscience, San Jose, CA, USA). EdU-positive or GFP-EdU-positive cells were gated, and their DNA content was compared to the total cell population. The proportion of dividing cells within these gated populations was quantified at designated time points.

2.14. Data analysis

Data analysis was performed using GraphPad Prism 9.0 (GraphPad, La Jolla, CA, USA) or IBM SPSS Statistics 20 (SPSS Science Inc., Chicago, IL, USA). Quantitative data are expressed as mean ± standard error of mean (SEM). For two-group comparisons, Student's *t*-test was used for normally distributed data with equal variance. For multiple independent groups, one-way ANOVA was applied. If normality or homogeneity assumptions were not met, data were log-transformed. If the transformation failed to satisfy these assumptions, the Mann−Whitney U test or Kruskal−Wallis H test was used for 2 or more groups, respectively. Categorical variables were summarized as frequencies and percentages, analyzed using the chi-square or Fisher's exact test, as appropriate. A two-tailed $P < 0.05$ was considered statistically significant. Multivariable analysis was conducted to calculate ORs and 95% confidence intervals.

3. Results

3.1. PPE was associated with abnormal neurodevelopment in infants, particularly communication skills

We conducted a cross-sectional study to evaluate neurodevelopment in infants aged 6 to 24 months with PPE, using the ASQ:SE-2 and ASQ-3 questionnaires (Fig. 1A). Baseline characteristics (Supporting Information Tables S3 and S4) revealed no significant differences among the normal control group (Control), the autoimmune disease PPE group (median dose: 10 mg/day), and the autoimmune disease prenatal prednisone non-exposed (PPNE) group in maternal gestational age, pregnancy-related conditions, delivery timing, or infant anthropometrics. For male infants, ASQ:SE-2 scores were significantly higher in 12 to 24-month PPE group compared to the other groups, with no differences at 6 months (Fig. 1B). Chi-square analysis confirmed a higher proportion of abnormal ASQ:SE-2 scores in this subgroup (Fig. 1C). ASQ-3 analysis showed that male infants in the PPE group scored significantly lower in communication and fine motor skills compared to other groups, with gross motor, problem-solving, and personal-social domains also being significantly reduced relative to the control group (Fig. 1D). A higher proportion of infants in the PPE group scored "below the cutoff" in communication and fine motor domains, with communication most severely affected (Fig. 1E).

Among female infants, ASQ:SE-2 scores were significantly elevated in the 18- and 24-month-old PPE group, although no differences were observed at 6 to 12 months (Fig. 1F). Chi-square analysis found no significant differences in the proportion of scores "at or above the cutoff" for the 18- and 24-month PPE groups (Fig. 1G). ASQ-3 analysis revealed significantly lower communication domain scores in PPE female infants compared to the other groups (Fig. 1H), with increased proportions of "below the cutoff" scores in communication and gross motor domains, particularly affecting communication (Fig. 1I).

Univariate and multivariate logistic regression analyses explored potential causes of these impairments. Univariate analysis associated abnormal ASQ:SE-2 scores with PDN exposure and maternal immune diseases, while ASQ-3 communication deficits were linked to PDN exposure, maternal immune diseases, age, and gestational diabetes. Multivariate analysis identified PPE as an independent risk factor for abnormal scores in both ASQ:SE-2 (odds ratio (OR) = 5.02, $P = 0.013$) and ASQ-3 communication domains (OR = 5.27, $P = 0.012$) (Supporting Information Table S5). In conclusion, PPE adversely impacts infant brain development, with communication deficits being particularly pronounced in both sexes. These findings highlight potential disruptions in specific brain regions associated with communication skills.

3.2. PPE induced anxiety- and depression-like behaviors in adult offspring rats, accompanied by cortical nerve cells reduction and structural abnormalities

Fluctuations in reproductive hormone levels profoundly influence women's mental health, regulating numerous neurotransmitters in the brain. These hormonal changes, combined with individual sensitivity to environmental factors, contribute to the onset and progression of affective disorders[28-30]. To more accurately assess the long-term impact of PPE on offspring neurodevelopment, offspring rats (postnatal week 12, PW12) underwent a series of behavioral tests designed to evaluate motor function, anxiety, depression, and cognitive abilities. In the open field test (OFT), PPE male offspring spent significantly less time in the center area, while overall locomotor activity remained unchanged compared to controls (Fig. 2A). This suggests that PPE reduced exploratory behavior, indicating potential anxiety-like tendencies. In the elevated plus maze (EPM), PPE male offspring preferred the closed arms, spending significantly less time in the open arms (Fig. 2B), further supporting anxiety-like behavior. Additionally, in the novelty suppressed feeding test (NSFT), PPE male offspring exhibited a prolonged latency to feed, consistent with anxiety-related traits (Fig. 2C). Depression-like behaviors were assessed using the forced swimming test (FST) and sucrose preference test (SPT). FST results showed increased immobility time in PPE male offspring, reflecting despair-like behavior (Fig. 2D). In the SPT, PPE male offspring consumed less sucrose, indicative of anhedonia, a core symptom of depression (Fig. 2E). It is noteworthy that female offspring subjected to PPE did not show significant anxiety- or depression-like phenotypes (Supporting Information Fig. S1A−S1C). This observation aligns with clinical evidence

(TBR1, green, deep-layer neuronal marker), and quantitative analysis. Scale bar = 500 μm; white dashed rectangles indicate magnified regions. Scale bar = 50 μm, $n = 5$. (K) mRNA expression levels of microtubule-associated protein 2 (*Map2*), $n = 8$. (L) mRNA expression levels of *Gfap* and immunofluorescence images for GFAP (astrocytic marker). Scale bar = 100 μm. Data are presented as mean ± SEM; $^{*}P < 0.05$, $^{**}P < 0.01$ *vs.* respective Control.

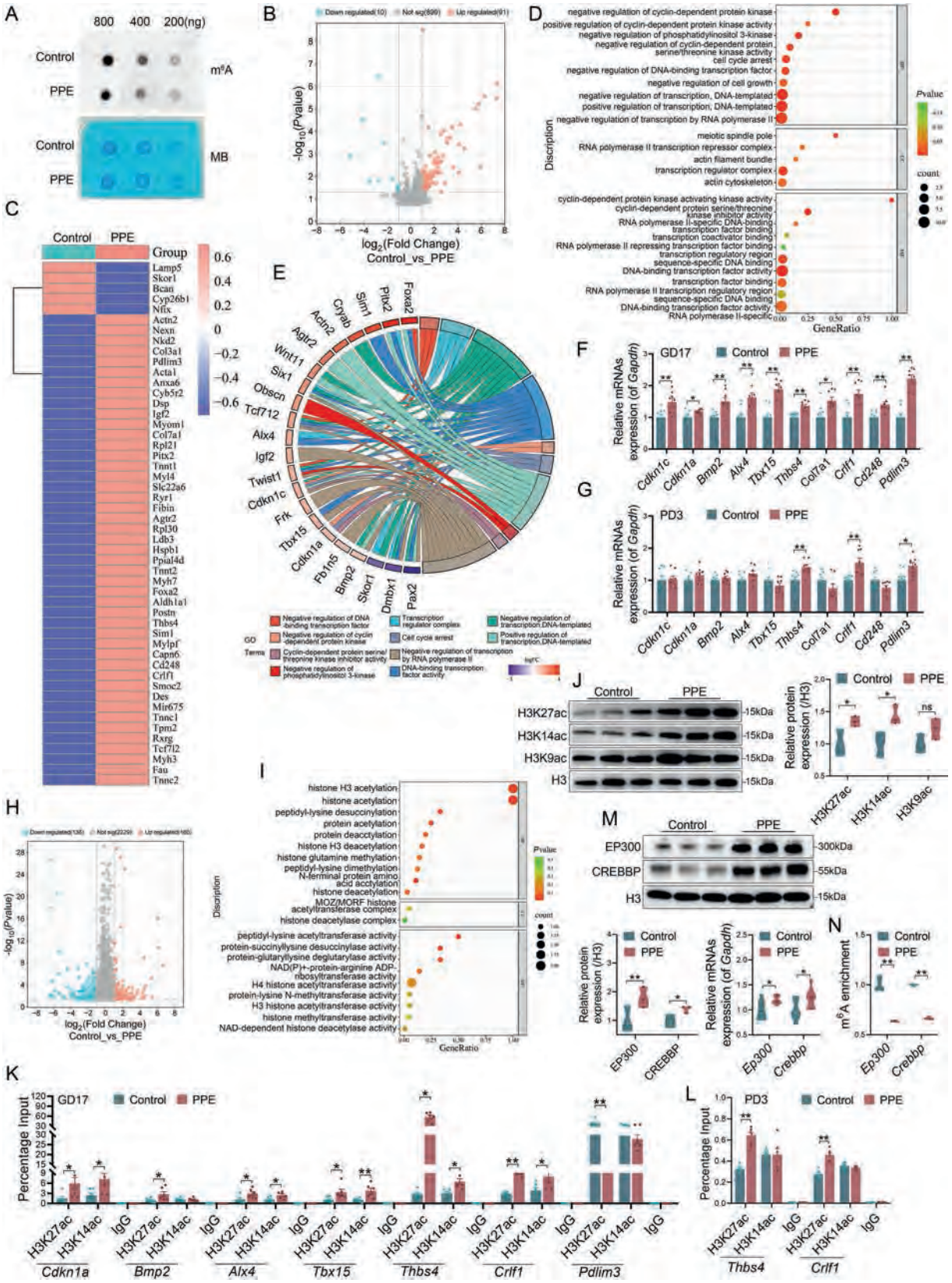

Figure 5 N^6-Methyladenosine (m^6A) regulated cell cycle and neuronal differentiation gene expression in PPE offspring rat RGCs histone 3 lysine 27 acetylation (H3K27ac) modification. (A) Dot blot analysis of m^6A modification in total RNA from GD17 fetal rat cortices. (B) Volcano plot showing significantly altered mRNA expression. (C) Heatmap displaying the top 50 genes with significantly altered mRNA expression. (D) Gene ontology (GO) enrichment analysis of changed mRNAs. (E) Chord diagram illustrating the enrichment of differentially altered genes in the top 10 GO pathways. (F), (G) Real-time quantitative PCR (RT-qPCR) analysis of differential genes related to cell cycle and neuronal

indicating that the adverse neurobehavioral effects of PPE are more prominent in males. Accordingly, our subsequent investigations concentrated on male offspring. In addition, no significant differences between PPE and control offspring were observed in spatial learning and memory, as assessed by the novel object recognition test (NORT), suggesting that PPE primarily affects emotional rather than cognitive functions (Fig. 2F).

Neurons and non-neuronal cells, such as glial cells, play critical roles in regulating neural system function and the pathogenesis of psychiatric disorders[31]. To investigate the underlying neurobiological mechanisms, we analyzed cortical development in PPE offspring. NeuN immunostaining revealed a significant reduction in mature neurons in the cortex (Fig. 2G). Additionally, synaptic markers—SNAP25, PSD-95, and SHANK3—were significantly lower in the PPE group (Fig. 2H), indicating synaptic structural deficits. Transmission electron microscopy (TEM) further revealed significant synaptic alterations, including reduced postsynaptic density (PSD) thickness, widened synaptic clefts, shortened active zone lengths, and a lower number of synapses (Fig. 2I), confirming synaptic structural impairments. Furthermore, a significant reduction in astrocytes was observed in the PPE offspring cortex (Fig. 2J). Structural analysis revealed significant astrocytic abnormalities, including decreased branch length, volume, and number (Fig. 2J), suggesting compromised astrocyte function.

In summary, PPE led to a reduction in cortical neurons and synaptic impairments, as well as abnormalities in astrocyte numbers and morphology. These cellular and structural alterations align with the anxiety- and depression-like behaviors observed in the behavioral tests, providing histological evidence of neurodevelopmental impairments induced by PPE.

3.3. PPE impaired cortical neurogenesis in offspring by suppressing RGCs proliferation and differentiation

Cortical development in mammals relies heavily on the active proliferation and differentiation of RGCs. As pivotal neural stem cells, RGCs generate intermediate progenitor cells (IPCs) and neurons, contributing to the laminar structure of the cortex[32]. During the perinatal period, RGCs' activity declines, leading to reduced neurogenesis and a shift toward gliogenesis[33]. Therefore, we hypothesize that the reduced cortical nerve cells in adult PPE offspring are linked to abnormal RGCs proliferation and differentiation.

RGCs are progressively depleted in the mouse cortex during early postnatal development. In line with the developmental timelines of rats and mice, postnatal day 3/10 (PD3/PD10) were chosen as critical time points for analysis. PD3 marks the transition of RGCs into astrocytes[34], while PD10 represents near-complete depletion of RGCs[35]. Our results showed significant reductions in both cortical area and thickness in PPE offspring at PD3 and PD10 compared to controls (Fig. 3A and B).

Further analysis revealed that the mRNA levels of *Pax6,* a marker of RGC, were significantly reduced in the cortices of PPE offspring, along with a marked decrease in PAX6-positive cells (Fig. 3C and D). BrdU/PAX6 dual-labeling experiments showed that RGCs proliferation was accelerated in the PPE group, shortening their proliferative cycle and leading to an earlier depletion of the RGCs pool (Fig. 3D). This suggests that PPE exposure accelerates RGCs depletion, thereby impairing cortical neurogenesis during the neonatal period.

To validate this hypothesis, we assessed markers for mature neurons and astrocytes in neonatal cortices. The mRNA expression of *Rbfox3* and *Gfap* was significantly reduced in PPE offspring (Fig. 3E and F). Immunofluorescence staining revealed a substantial decrease in the density of mature neurons and astrocytes in the PPE group (Fig. 3G–J).

In summary, PPE significantly impairs the proliferation and differentiation of RGCs in offspring, leading to defects in neonatal cortical neurogenesis. These early disruptions likely contribute to the reduced nerve cell populations and structural abnormalities observed in adulthood, which may underlie the anxiety- and depression-like behaviors observed.

To investigate the origins of the cortical nerve cells deficits and cortical reduction induced by PPE, we examined changes in embryonic RGCs. Based on the developmental timeline of RGC in mice and rats, we selected gestational day 17 (GD17, a stage where RGCs predominantly differentiate into neurons) and GD20 (a stage where RGCs begin differentiating into astrocytes) as critical observation points[36]. At both GD17 and GD20, cortical area and thickness were significantly reduced in PPE offspring compared to controls (Fig. 4A and B). Real-time quantitative PCR (RT-qPCR) and immunofluorescence analyses revealed a marked decrease in *Pax6* mRNA expression (Fig. 4C) and a significant reduction in the thickness of PAX6-positive cells along the ventricular zone (Fig. 4D and E). Concurrently, the mRNA levels of *Eomes* (encoding TBR2) were also significantly reduced (Fig. 4F), further indicating impaired RGCs proliferation and differentiation.

The reduction in cortical area suggested abnormalities in neurogenesis. To explore this, we performed fluorescence staining for CTIP2 (a marker of deep-layer neurons in layers V–VI) and CUX1 (a marker of upper-layer neurons in layers II–IV) in brain sections from GD17 and GD20. At GD17, the thickness of upper-layer neurons was significantly increased, while deep-layer neuron thickness was markedly reduced in the PPE group (Fig. 4G and H). By GD20, both upper- and deep-layer neuron thicknesses were significantly thinner in PPE offspring (Fig. 4G and H). These findings suggest that PPE may prematurely induce RGCs differentiation, resulting in a shortened proliferative cycle and impaired later-stage neurogenesis.

To further confirm this, brain sections from GD20 with TBR1 (a marker of deep-layer neurons) and SATB2 (a marker of upper-layer neurons) staining confirmed significant reductions in both deep- and upper-layer neurons in the PPE group (Fig. 4I and J). The expression of the mature neuronal marker *Map2* was also

differentiation, $n = 8$. (H) Volcano plot showing differential methylation peaks. (I) GO enrichment analysis of histone modification-associated differential methylation peaks. (J) Representative Western blot images and quantification of H3K27ac, histone 3 lysine 14 acetylation (H3K14ac), and histone 3 lysine 9 acetylation (H3K9ac) levels in nuclear proteins, $n = 3$. (K), (L) Chromatin immunoprecipitation (ChIP)-qPCR assay showing the expression of H3K27ac and H3K14ac at the promoters and enhancers of cell cycle and neuronal differentiation-related differential genes, $n = 6$. (M) Representative Western blot images and quantification of nuclear protein levels of cAMP response element-binding protein CREB binding protein (CREBBP) and E1A binding protein p300 (EP300), $n = 3$; mRNA expression levels of *Crebbp*/*Ep300*, $n = 8$. (N) Comparison of m^6A-MeRIP-qPCR for *Crebbp*/*Ep300*, $n = 5$. Data are presented as mean ± SEM; $^*P < 0.05$, $^{**}P < 0.01$ *vs.* respective Control.

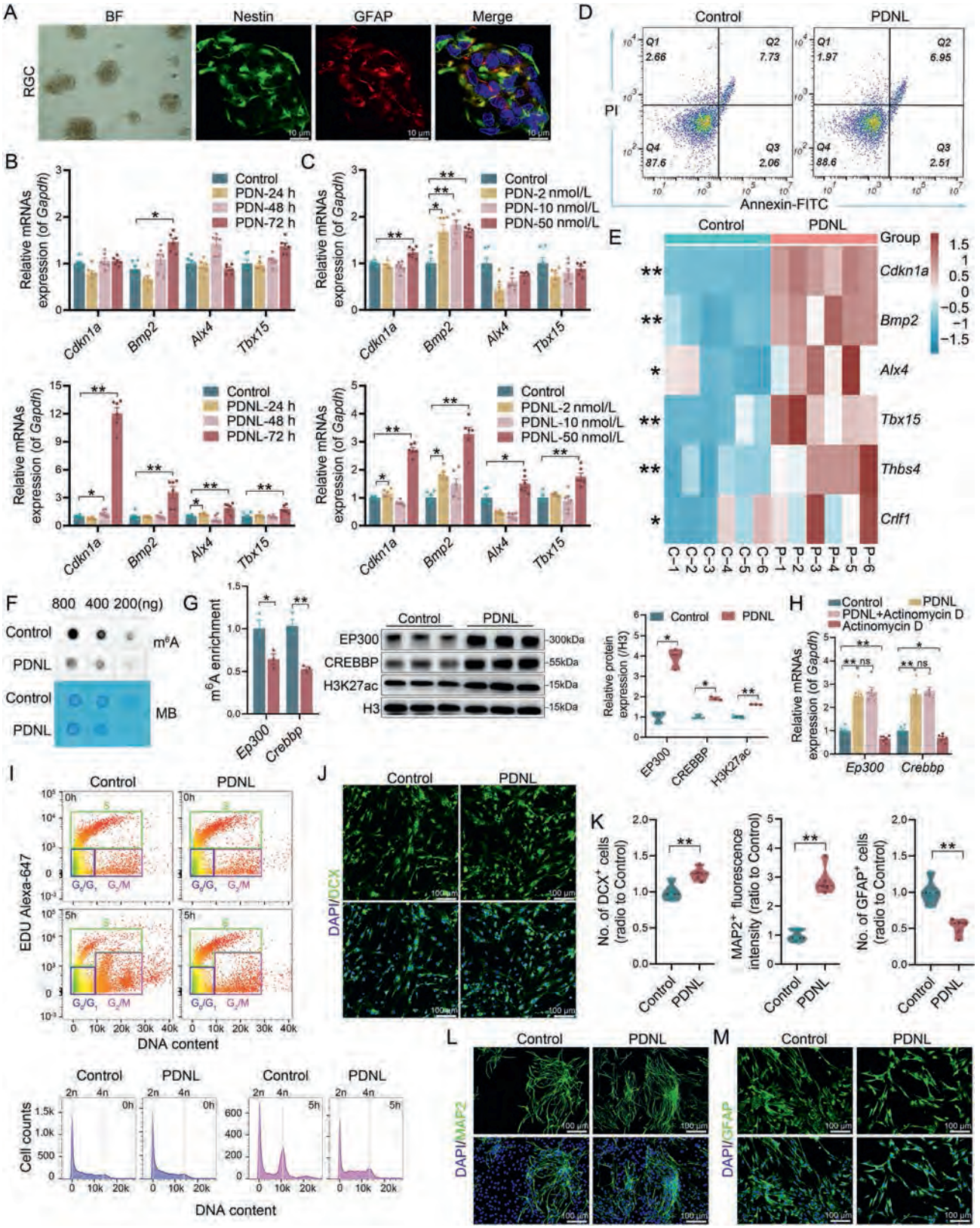

Figure 6 Prednisolone (PDNL) inhibited RGCs' proliferation and differentiation *via* m^{6}A-regulated H3K27ac modifications. (A) Suspension culture of RGCs' spheres derived from fetal rat cortical tissue after 5−7 days, validated with Nestin (green) and GFAP (red) immunofluorescence staining. (B), (C) Time- and dose-dependent effects of prednisone (PDN) and PDNL treatments on primary RGCs, $n = 6$. (D) Flow cytometry analysis of apoptosis in RGCs. (E) Gene expression levels of cell cycle- and neuronal differentiation-related genes, $n = 6$. (F) Dot blot analysis of total RNA m^{6}A levels, $n = 3$. (G) Comparison of m^{6}A-MeRIP-qPCR for *Crebbp*/*Ep300*, $n = 3$. Representative images and quantification of

significantly downregulated in PPE offspring at GD17 and GD20 (Fig. 4K). Additionally, the density of astrocytes and *Gfap* mRNA expression were markedly reduced in the PPE group (Fig. 4L).

In conclusion, PPE disrupts cortical neurogenesis by impairing the proliferation and differentiation of embryonic RGCs. These abnormalities are evident as early as the intrauterine stage, persist postnatally, and ultimately lead to reduced cortical nerve cells and functional impairments in adult offspring.

3.4. m^{6}A modification mediated PPE-induced RGCs proliferation and differentiation impairments via H3K27ac regulation

m^{6}A is the most abundant RNA modification and plays a critical role in regulating neurodevelopment. Using MeRIP-Seq analysis of cortical tissues from GD17 fetal rats, we identified the canonical m^{6}A motif sequence GGACA (Supporting Information Fig. S2A). Dot blot analysis confirmed a significant reduction in m^{6}A modification levels in the PPE group (Fig. 5A). Distribution analysis revealed that m^{6}A peaks were primarily localized around stop codons and 3′UTR regions, with a similar distribution of functional gene elements between groups (Fig. S2B and S2C). However, changes in m^{6}A modification levels were not strongly correlated with mRNA expression levels (Fig. S2D), suggesting an indirect regulatory mechanism. Transcriptome analysis revealed significant upregulation of gene expression in the cortex of PPE offspring (Fig. 5B). Among the top 50 most altered genes, 8 genes (*Thbs4*, *Col7a1*, *Crlf1*, *Cd248*, *Pdlim3*, *Sim1*, *Agtr2*, *Igf2*) were closely related to nervous system development (Fig. 5C). Gene ontology (GO) enrichment analysis showed significant enrichment in cell cycle-related pathways (Fig. 5D). Further screening identified 13 cell cycle-associated genes (*Cdkn1c*, *Cdkn1a*, *Bmp2*, *Alx4, Tbx15*, *Pitx2*, *Foxa2*, *Six1*, *Tcf12*, *Skor1*, *Dmbx1*, *Pax2*, *Wnt11*) (Fig. 5E). RT-qPCR validation demonstrated that the expression changes of 5 neuronal differentiation-related genes (*Thbs4*, *Col7a1*, *Crlf1*, *Cd248*, *Pdlim3*) and 5 cell cycle-associated genes (*Cdkn1c*, *Cdkn1a*, *Bmp2*, *Alx4*, *Tbx15*) were consistent with the transcriptome results (Fig. 5F and S2E). Analysis of gene expression patterns in the PD3 and PD10 offspring cortex showed no significant changes in cell cycle-related gene expression during the neonatal period (Fig. 5G), suggesting that RGCs proliferation abnormalities primarily occurred prenatally. At PD3, the expression patterns of neuronal differentiation-related genes (*Thbs4*, *Crlf1*, *Pdlim3*) aligned with those at GD17. However, by PD10, these differences were no longer significant (Fig. S2F), likely due to RGCs differentiation into astrocytes before their depletion.

Analysis of m^{6}A peak distribution revealed 160 upregulated and 138 downregulated genes among the top 1000 genes in the PPE fetal cortex (Fig. 5H). Considering the pivotal role of histone tail modifications in regulating gene expression[37], GO analysis highlighted significant enrichment in histone acetylation pathways, particularly those involving H3 acetylation (Fig. 5I). Western blot analysis revealed increased H3K27ac and H3K14ac levels in the PPE group cortex, while H3K9ac levels remained unchanged (Fig. 5J). Chromatin immunoprecipitation (ChIP)-qPCR further demonstrated that prenatal changes in H3K27ac were positively correlated with the expression of four cell cycle-associated genes and three neuronal differentiation genes, while H3K14ac correlated with 3 cell cycle genes and 2 neuronal differentiation genes (Fig. 5K and S2G). Analysis of PD3 offspring indicated that PPE-induced changes in neuronal differentiation gene expression were primarily associated with H3K27ac modifications (Fig. 5L). ChIP-qPCR verification of H3K9ac revealed no correlation with target gene expression changes (Fig. S2H). To explore the molecular mechanism underlying H3K27ac modifications, we examined the expression of H3K27ac transferases *Crebbp*/*Ep300*. PPE offspring showed significantly elevated mRNA and protein levels of CREBBP/EP300 in the cortex (Fig. 5M). The presence of m^{6}A in *Crebbp*/*Ep3*00 mRNA was assessed using MeRIP-qPCR. The results showed a decreased enrichment of m^{6}A in *Crebbp*/*Ep3*00 mRNA in the cortex of PPE offspring (Fig. 5N). These findings suggest that the loss of m^{6}A modification may stabilize *Crebbp*/*Ep3*00 mRNA, leading to elevated H3K27ac levels and subsequent regulation of cell cycle and neuronal differentiation genes.

To validate the MeRIP-Seq results in cortical RGC, primary RGC were isolated from fetal cortical tissue for further analysis (Fig. 6A). Prednisolone (PDNL), the active metabolite of PDN[38], was used for *in vitro* experiments at concentrations of 2, 10, and 50 nmol/L, reflecting fetal blood levels in the PPE model (PDN: 11.6 ± 9.9 nmol/L, PDNL: 23.8 ± 25.1 nmol/L). Time- and dose-dependent analyses revealed that 50 nmol/L PDNL treatment for 72 h induced mRNA expression changes in cell cycle-related genes similar to the findings in animal tissues (Fig. 6B and C). Flow cytometry confirmed that this concentration did not induce apoptosis in RGCs (Fig. 6D), excluding apoptosis as a factor in the reduced RGCs number. Heatmap analysis of gene expression demonstrated significant alterations in cell cycle- and neuronal differentiation-related genes in PDNL-treated RGCs (Fig. 6E), indicating that PDNL is a key factor in cortical neurogenesis impairment in the PPE model.

Dot blot assays revealed reduced m^{6}A modification levels in PDNL-treated RGCs (Fig. 6F). Further analysis revealed that PDNL treatment reduced the m^{6}A modification of *Ep300*/*Crebbp*, leading to increased mRNA and protein levels of CREBBP/EP300, as well as enhanced H3K27ac modification (Fig. 6G and H), thereby affecting genes associated with cell cycle regulation and neuronal differentiation. Moreover, treatment with Actinomycin D failed to reverse the PDNL-induced upregulation of *Ep300/Crebbp* mRNA, suggesting that transcriptional activation is unlikely to be involved in this process (Fig. 6H). EdU incorporation assays showed reduced RGCs proliferation, with delayed progression through the S−G2/M phase (Fig. 6I). Differentiation induction experiments revealed that PDNL treatment biased RGCs differentiation toward neurons, with increased numbers of DCX-

CREBBP/EP300, and H3K27ac levels in nuclear proteins, $n = 3$. (H) RT-qPCR analysis of the effects of PDNL and Actinomycin D on *Crebbp*/*Ep3*00 mRNA levels, $n = 6$. (I) Flow cytometry analysis of RGCs cell cycle progression. Top: Dot plots at 0 h and 5 h post-5-ethynyl-2′-deoxyuridine (EdU) pulse. Specific cell cycle phases are indicated in boxed regions. Bottom: Histograms of DNA content for EdU-positive and total cell populations. Confocal images and quantification of doublecortin (DCX) (J), MAP2 (L), and GFAP (M) with quantitative analysis (K). Scale bar = 100 μm, $n = 5$. Data are presented as mean ± SEM; ns, no significance; $^*P < 0.05$, $^{**}P < 0.01$ *vs.* respective Control.

and MAP2-positive neurons and fewer GFAP-positive astrocytes (Fig. 6J−M), consistent with *in vivo* observations.

Based on these findings, it is hypothesized that genes such as *Cdkn1a*, *Bmp2*, *Alx4*, and *Tbx15* may regulate RGCs cell cycle progression, whereas *Thbs4* and *Crlf1* may influence neuronal differentiation.

To further evaluate the role of H3K27ac modifications in RGCs cell cycle and differentiation, we used lentiviral shRNA to knock down *Ep300*. After 72 h, successful knockdown of *Ep300* was confirmed by green fluorescent protein (GFP) expression and RT-qPCR (Supporting Information Fig. S3A). *Ep300* depletion significantly reduced nuclear H3K27ac levels in PDNL-treated RGCs, confirming that PDNL regulates H3K27ac *via Ep300* (Fig. S3B). RT-qPCR revealed partial restoration of target gene expression following *Ep300* knockdown (Fig. S3C). Immunofluorescence analysis showed that following *Ep300* knockdown intervention, the numbers of newborn neurons (Fig. S3D) and mature neurons (Fig. S3E and S3F) in the PDNL + shRNA group were significantly reduced compared to the PDNL + NC group, while the number of astrocytes increased (Fig. S3G and S3H). These findings indicate that *Ep300* knockdown mitigates the PDNL-induced bias in RGCs' differentiation toward neuronal lineage. Proliferation assays revealed that the delay in S−G2/M phase progression observed in primary RGCs of the PDNL + shRNA group was notably alleviated (Fig. S3I), and the EdU-positive cell population was significantly increased (Fig. S3J), indicating that *Ep300* knockdown effectively rescued the cell cycle abnormalities caused by PDNL.

In summary, PPE-induced m^{6}A depletion modification stabilizes the mRNA expression of *Crebbp*/*Ep300*, increases H3K27ac modification levels, and activates the expression of genes associated with cell cycle arrest and neuronal differentiation, leading to abnormal proliferation and differentiation of RGCs, ultimately causing cortical neurogenesis defects.

3.5. FTO regulated m^{6}A to enhance H3K27ac modifications in cortical RGCs of PPE offspring

The m^{6}A modification is catalyzed by methyltransferases (*e.g.*, METTL3, METTL14, WTAP) and removed by demethylases (*e.g.*, FTO and ALKBH5)[39]. Our results revealed a significant upregulation of *Fto* expression in the cortex of PPE offspring (Supporting Information Fig. S4A), while expression levels of *Mettl3*, *Mettl14*, *Wtap*, and *Alkbh5* remained unchanged. This suggests that *Fto* may contribute to reduced m^{6}A levels in RGCs of PPE offspring. Additionally, nuclear expression of FTO protein increased, whereas cytoplasmic expression decreased (Fig. S4B), indicating PPE-induced translocation of FTO from the cytoplasm to the nucleus. This was further confirmed in primary RGC treated with PDNL (Fig. S4C).

To further explore FTO's role, we overexpressed *Fto* (*Fto^{oe}*) in primary RGC using lentiviral transduction. After 72 h, GFP expression was significantly increased (Supporting Information Fig. S5A). RT-qPCR and Western blot confirmed successful overexpression of FTO (Fig. S5B). Dot blot analysis showed that *Fto^{oe}* significantly decreased m^{6}A levels in primary RGC, confirming FTO's negative regulation of m^{6}A modification (Fig. S5C). Moreover, in the *Fto^{oe}* group, the enrichment of m^{6}A in *Crebbp*/*Ep300* mRNA in primary RGC decreased (Fig. S5D). *Fto^{oe}* promoted nuclear accumulation of CREBBP/EP300 mRNA and protein, accompanied by increased H3K27ac modifications (Fig. S5E).

Further analysis revealed that *Fto^{oe}* significantly upregulated genes related to the cell cycle and neuronal differentiation in RGC (Fig. S5F). Flow cytometry revealed that *Fto^{oe}* extended the S−G2/M phase, inhibiting RGCs proliferation (Fig. S5G). Immunofluorescence staining demonstrated a significant increase in newborn and mature neurons, alongside a reduction in astrocytes (Fig. S5H−S5K). In summary, FTO regulates m^{6}A modifications and influences H3K27ac levels, impairing RGCs proliferation and differentiation. This mechanism is likely a key factor underlying the suppression of RGCs proliferation and differentiation in the cortical development of PPE offspring.

To validate whether PPE inhibits RGCs proliferation and differentiation through FTO regulation, we employed CRISPR-Cas9 gene-editing technology to generate *Fto$^{fl/fl}$*; Nestin-Cre cKO mice. Compared to the Control-wild type (C-WT) group, the PPE-wild type (PPE-WT) group showed significantly reduced cortical area and thickness. However, both were significantly restored in the PPE-cKO group, approaching the levels observed in the Contorl-cKO (C-cKO) group (Fig. 7A and B), indicating that specific deletion of *Fto* blocks PPE's effects.

Pathological analysis confirmed these findings. Immunofluorescence and RT-qPCR showed that, in the C-WT group, RGCs were aligned along the ventricular wall. In contrast, RGCs alignment and *Pax6* expression were significantly reduced in the PPE-WT group (Fig. 7C and D). In the PPE-cKO group, RGCs alignment and *Pax6* expression were partially restored, indicating that *Fto* deletion alleviated PPE-induced inhibition of RGCs proliferation. Moreover, the PPE-cKO group exhibited an increased number of RGCs and IPCs upregulation of *Eomes* (Fig. 7E). In the PPE-WT group, both deep- and upper-layer neuron numbers were significantly reduced, whereas the PPE-cKO group demonstrated restoration of neuron density across cortical layers (Fig. 7F and G). Additionally, *Map2* mRNA expression was significantly increased in the PPE-cKO group (Fig. 7H). The differentiation of astrocytes was also improved, with the expression level of *Gfap* mRNA in the PPE-cKO group restored to levels similar to those in the C-cKO group (Fig. 7I).

We further examined m^{6}A modifications in *Fto$^{fl/fl}$*; Nestin-Cre cKO mice. Compared to the C-WT group, the C-cKO group exhibited significantly elevated m^{6}A levels (Fig. 7J), confirming successful *Fto* deletion. In the PPE-WT group, m^{6}A levels were markedly reduced. Still, they were restored in the PPE-cKO group to levels similar to the C-cKO group, confirming that PPE primarily exerts its effects by regulating FTO and reducing m^{6}A levels. The enrichment of m^{6}A in *Crebbp*/*Ep300* mRNA in the cortex of PPE-ckO offspring was increased (Fig. 7K). Further analysis showed decreased CREBBP/EP300 mRNA and protein expression in the PPE-cKO group, accompanied by reductions in H3K27ac modifications (Fig. 7L and M). Genes associated with the cell cycle and neuronal differentiation were significantly upregulated in the PPE-WT group but partially restored in the PPE-cKO group (Fig. 7N), alleviating PPE-induced suppression of RGCs proliferation and differentiation.

In conclusion, FTO plays a pivotal role in PPE's effects on cortical RGC. Specific deletion of *Fto* effectively disrupts PPE-induced m^{6}A dysregulation, partially restores RGCs proliferation and differentiation, and ameliorates cortical neurogenesis deficits.

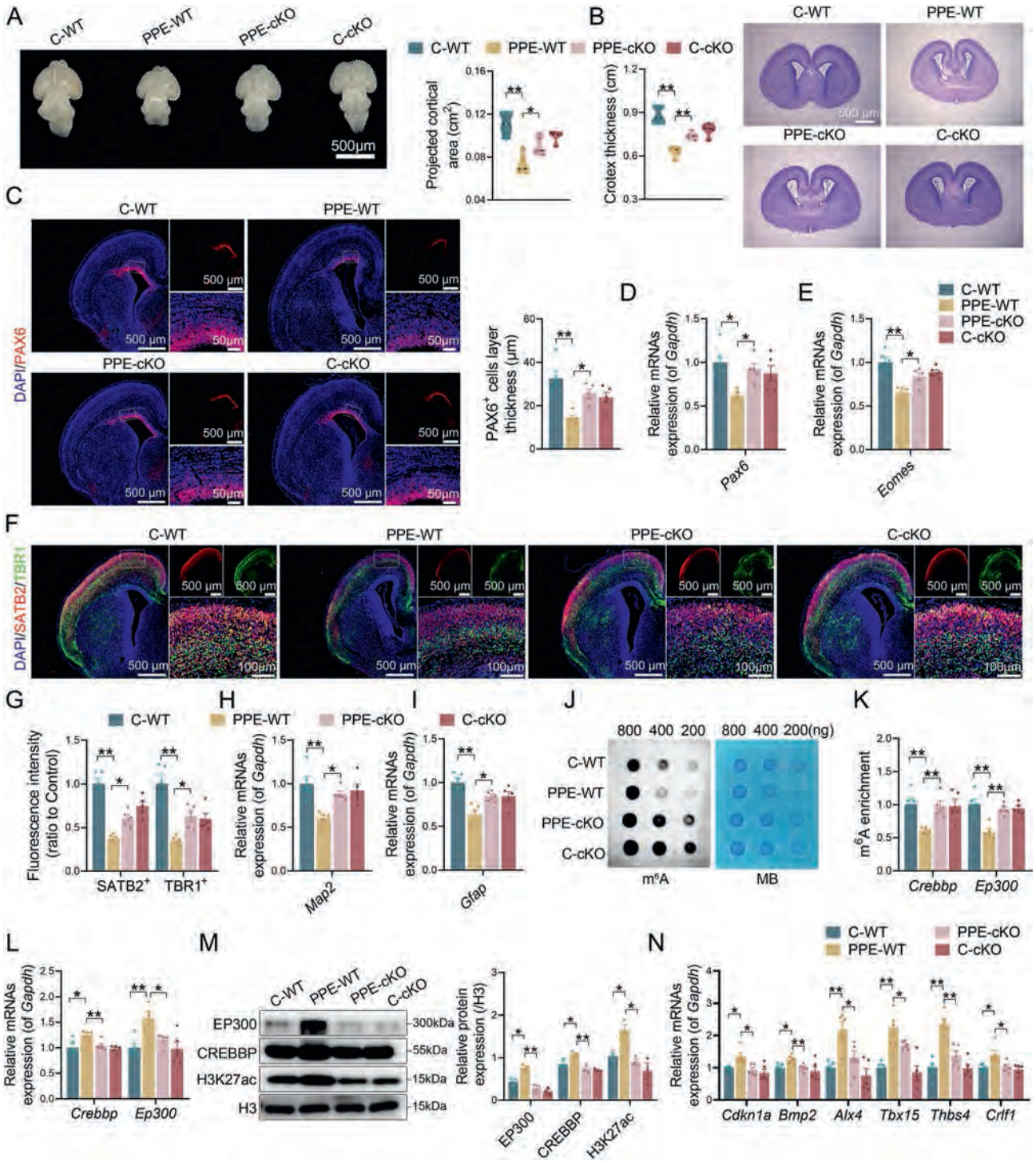

Figure 7 Fat mass and obesity associated protein (*Fto*) knockout restored m^{6}A levels and rescued PPE-induced RGCs proliferation and differentiation deficits. (A) Images and quantification of cortical area in GD18 wild-type and *Fto*$^{fl/fl}$; Nestin-Cre fetuses. Dashed lines represent the cortical area. Scale bar = 500 μm, $n = 5$. (B) HE staining and quantification of cortical thickness. Scale bar = 500 μm, $n = 5$. (C) Representative images of PAX6 immunofluorescence staining and quantification. Scale bar = 500 μm. Enlarged region in dashed boxes. Scale bar = 50 μm, n = 5. (D) mRNA expression levels of *Pax6*, $n = 5$. (E) mRNA expression levels of *Eomes*, $n = 5$. (F) Coronal sections showing SATB2 (red) and TBR1 (green) staining and quantification (G). Scale bar = 500 μm; Enlarged region in dashed boxes. Scale bar = 100 μm, $n = 5$. mRNA expression levels of *Map2* (H) and *Gfap* (I), $n = 5$. (J) Dot blot analysis of m^{6}A levels, $n = 3$. (K) Comparison of m^{6}A-MeRIP-qPCR for *Crebbp*/*Ep300*, $n = 5$. (L) mRNA expression levels of *Crebbp/Ep300*, $n = 5$. (M) Representative images and quantification of CREBBP/EP300, and H3K27ac levels in nuclear proteins, $n = 3$. (N) RT-qPCR analysis of cell cycle and neuronal differentiation-related genes, $n = 5$. Data are presented as mean ± SEM; $^*P < 0.05$, $^{**}P < 0.01$ *vs.* C-WT or PPE-cKO.

3.6. Early postnatal NRG-1 intervention mitigated PPE-induced neurogenesis deficits and anxiety- and depression-like behaviors by promoting RGCs proliferation

NRG-1, a critical growth factor, plays a pivotal role in regulating neuroepithelial cell proliferation during neurodevelopment[40]. This study investigated whether NRG-1 supplementation could promote RGCs proliferation and mitigate PPE-induced cortical neurogenesis impairments.

In the Control + NRG-1 (Control_N) group, NRG-1 showed no apparent toxicity. At PD10, the PPE + NRG-1 (PPE_N) group exhibited significant increases in brain area and cortical thickness at PD10 (Fig. 8A and B), with no significant changes at PD3, likely due to treatment frequency and RGCs proliferation cycles. RT-qPCR and immunofluorescence staining revealed that PAX6 expression and PAX6 domain thickness were significantly increased in the PPE_N group compared to the PPE + saline (PPE_S) group (Fig. 8C and D), indicating that NRG-1 stimulated RGC proliferation. Further analysis showed a substantial increase in mature neurons and astrocytes in the PPE_N group (Fig. 8E−H), suggesting partial restoration of neurogenesis.

In adult offspring, the PPE_N group showed a higher number of cortical neurons and increased mRNA levels of synaptic markers *Snap25*, *Dlg4* (encoding PSD-95), and *Shank3* (Fig. 8I and J). TEM revealed significant improvements in synaptic ultrastructure along with an increased synapse number (Fig. 8K−N), and astrocyte structural restoration was confirmed by Sholl analysis (Fig. 8O and P). Behavioral evaluations indicated that NRG-1 alleviated anxiety- and depression-like behaviors (Supporting Information Fig. S6A−S6E).

In summary, early postnatal NRG-1 intervention promoted RGCs proliferation, rescued PPE-induced neurogenesis deficits, and alleviated anxiety- and depression-like behaviors, highlighting NRG-1's potential therapeutic value.

4. Discussion

PDN is a commonly used glucocorticoid for pregnant patients with autoimmune inflammatory diseases like systemic lupus erythematosus and rheumatoid arthritis. In physiological conditions, PDN is converted into its active form, prednisolone, by 11β-hydroxysteroid dehydrogenase 1 (11β-HSD1) in the liver[41]. During pregnancy, placental 11β-HSD2 can convert prednisolone back to PDN, but around 10% of prednisolone crosses the placental barrier[42,43]. Additionally, during pregnancy, the elevated levels of corticosteroid-binding globulin further increase its binding ratio with PDN and PDNL[38], leading to passive fetal exposure to high concentrations of glucocorticoids, which poses a potential risk for adverse pregnancy outcomes.

This study integrates clinical cohort data with animal models to reveal the long-term effects of PPE on offspring neurodevelopment. Using ASQ:SE-2 and ASQ-3 questionnaires, we identified significant neurodevelopmental abnormalities, particularly in communication skills, in PPE infants and toddlers. These findings are consistent with previous studies linking prenatal glucocorticoid exposure to cognitive deficits[44]. Our results further confirm the detrimental impact of PPE on CNS development, particularly neurodevelopmental abnormalities, which are hallmarks of neurological dysfunction and closely linked to psychiatric disorders like depression, anxiety, schizophrenia, and attention-deficit/hyperactivity disorder[45-48]. Animal experiments corroborated these findings. PPE offspring displayed anxiety- and depression-like behaviors, reduced exploratory behavior, and increased despair in adulthood. Moreover, the cortical thickness was significantly reduced, paralleling neuroimaging findings in human depression[49,50]. These results suggest that cortical thinning may be a central feature of PPE-induced neurodevelopmental abnormalities, contributing to anxiety- and depression-like behaviors in adult offspring. Notably, emotional disorders such as anxiety and depression are often accompanied by deficits in social interaction and communication. Therefore, we speculate that the decline in communication skills observed in PPE infants may represent a potential risk factor for the development of language disorders in adulthood, which may exacerbate anxiety and depressive symptoms.

Cortical neurogenesis deficits arise from impaired proliferation and differentiation of RGCs, which are the primary source of cortical neurons and glial cells[51,52]. Our study found that PPE prolonged the RGCs cell cycle, inhibited their proliferation, and reduced the densities of both deep- and upper-layer neurons, as well as astrocytes. PPE also disrupted RGC differentiation, causing premature neuronal differentiation, depletion of RGC resources, and a decline in neuronal densities across cortical layers. The reduction in astrocytes likely resulted from impaired RGC proliferation. Our research shows that RGC neurogenesis is regulated by multi-layered epigenetic mechanisms, consistent with findings on m^{6}A RNA modifications in embryonic neural stem cells[33]. Yoon et al.[34] found that m^{6}A RNA modification regulates histone modifications, influencing neural stem cell fate and differentiation, highlighting the critical role of RNA-chromatin interaction in neurogenesis. Similarly, our work reveals that PPE affects cortical neurogenesis through the *Fto*−*Crebbp/Ep300*−H3K27ac epigenetic pathway, highlighting the importance of both RNA and histone modifications in regulating RGCs proliferation and differentiation. Additionally, research by Tiberi et al.[16] suggests that BCL6, through *Sirt1*-dependent regulation, also affects RGC fate and neurogenesis. Together, these findings underscore the pivotal role of epigenetic modifications in RGC development.

To further validate these mechanisms, we used an *Fto*$^{fl/fl}$; Nestin-Cre cKO mouse model. Under PPE, *Fto* deletion partially restored m^{6}A modification levels and significantly improved RGCs proliferation and differentiation, mitigating cortical neurogenesis deficits. These results highlight FTO's central role in m^{6}A regulation and its dysregulation as a key mediator of PPE-induced neurodevelopmental abnormalities. FTO has been identified as crucial for brain development, adult neurogenesis, and axonal regeneration[53,54]. Moreover, mutations in FTO are linked to severe neurodevelopmental disorders such as developmental delays, behavioral abnormalities, microcephaly, and other complex phenotypes[55]. Our findings suggest that PPE disrupts m^{6}A homeostasis by upregulating FTO expression and nuclear recruitment, leading to altered H3K27ac modifications and impaired RGCs function.

m^{6}A modification regulates neurodevelopment through multiple mechanisms, including precise control of mRNA stability, splicing, and translational efficiency. Mendel et al.[56] demonstrated that methyltransferase-like protein 16 (METTL16) increases m^{6}A labeling at the 3′ splice site of S-adenosylmethionine synthetase precursor mRNA, thereby inhibiting its proper splicing and protein production. YTHDC1 recognizes m^{6}A sites and recruits splicing factors (*e.g.*, SRSF3, SRSF10) to regulate splice site selection, influencing mRNA maturation[57]. In this study, we found

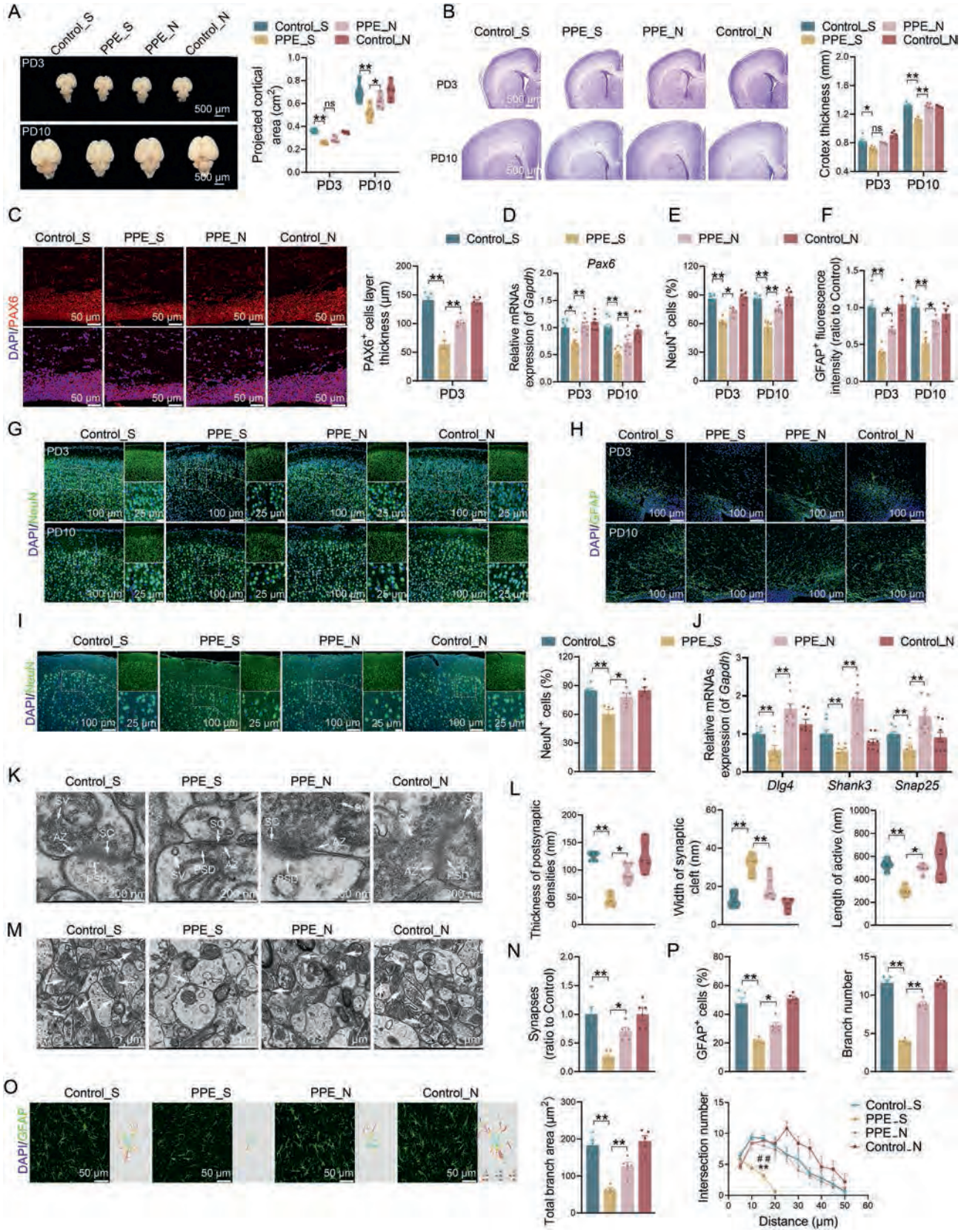

Figure 8 Early postnatal neuregulin-1 (NRG-1) intervention ameliorated cortical neurogenesis deficits in PPE offspring. (A) Images and quantification of the brain area in PD3 and PD10 offspring. Dashed lines represent the cortical area. Scale bar = 500 μm, $n = 5$. (B) HE-stained images and quantification of cortical thickness at PD3 and PD10. Scale bar = 500 μm, $n = 5$. (C) PAX6-positive cells at PD3 and PD10 with representative images and quantification. Scale bar = 50 μm, $n = 5$. (D) mRNA expression levels of *Pax6* at PD3 and PD10, $n = 8$. NeuN (E),

that PPE-induced reductions in m^{6}A on *Ep300* and *Crebbp* increased their mRNA stability, as confirmed by Actinomycin D treatment, which ruled out transcriptional activation. While m^{6}A may also affect splicing or translation, the parallel changes in mRNA and m^{6}A levels indicate that enhanced stability is the primary mechanism. Notably, PPE did not alter m^{6}A modification of RGC-related genes involved in the cell cycle (*Cdkn1a*, *Bmp2*, *Alx4*, *Tbx15*) or neuronal differentiation (*Thbs4*, *Crlf1*). These findings highlight a key role for m^{6}A-mediated stabilization of *Ep300* and *Crebbp* mRNA in driving the PPE-induced offspring phenotype.

NRG-1 is a key neurotrophic factor that regulates RGCs' proliferation, differentiation, and function during CNS development[40]. NRG-1 acts through erythroblastic leukemia viral oncogene homolog B (ErbB) receptors (ErbB2, ErbB3, ErbB4) to mediate neuronal and glial cell development. Previous studies indicate that NRG-1−ErbB2 interactions support RGCs' function and promote their differentiation into astrocytes[40]. In this study, we explored whether early postnatal NRG-1 supplementation could mitigate PPE-induced neurodevelopmental deficits. Our results demonstrated significant increases in mature neuron and astrocyte densities in both neonatal and adult PPE_N offspring, along with partial improvements in neuronal and astrocyte structural abnormalities. Additionally, anxiety- and depression-like behaviors were alleviated in PPE_N offspring, suggesting that NRG-1 exerts its therapeutic effects by restoring RGCs proliferation and differentiation.

Studies have shown that the AKT−mTOR signaling pathway regulates the expression of the m^{6}A methyltransferase METTL3, thereby affecting m^{6}A methylation modification[58]. Under physiological conditions, METTL3 primarily forms a complex with METTL14 to methylate mRNA, regulating gene expression and promoting neural stem cell proliferation[59]. It is known that NRG-1 can activate the AKT−mTOR pathway, suggesting that it may reverse PPE-induced m^{6}A loss by upregulating METTL3-mediated m^{6}A modification. Additionally, NRG-1 can activate multiple signaling cascades through the ErbB family, including PI3K−AKT, RAS−MAPK, PLCγ−PKC, and JAK−STAT pathways, whose kinases or transcription factors may further influence gene expression or protein activation related to histone acetylation or RNA methylation *via* cross-talk mechanisms[60-63]. Collectively, these findings suggest that NRG-1 has the potential to modulate epigenetic modifications to ameliorate neurocortical developmental deficits and anxiety- and depression-like behaviors in PPE-exposed offspring.

Notably, the timing of NRG-1 administration is critical. While early postnatal NRG-1 supplementation markedly improved neurogenesis and behavioral outcomes, administering NRG-1 after the completion of neurogenesis was less effective. This indicates that exogenous NRG-1 efficacy depends on active RGCs' proliferation and differentiation. Future studies should investigate optimal timing, dosages, and potential synergistic effects with other therapeutic strategies, such as m^{6}A- or H3K27ac-targeted interventions. In summary, this study provides the first evidence of the therapeutic potential of early postnatal NRG-1 supplementation in mitigating PPE-induced neurogenesis deficits. These findings highlight NRG-1 as a promising therapeutic agent for neurodevelopmental disorders related to prenatal glucocorticoid exposure, warranting further exploration in other neurodevelopmental conditions and combination therapies targeting epigenetic dysregulation.

The present study has certain limitations. It focused only on male offspring, neglecting potential sex-specific differences in neurodevelopment and behavior. Fluctuations in reproductive hormone levels profoundly impact women's mental health by modulating various neurotransmitters in the brain. These hormonal changes, combined with individual sensitivity to environmental factors, contribute to the onset and progression of mood disorders, which may underlie the differential vulnerability observed between female and male offspring[28-30]. Future studies should explore female offspring's developmental traits, considering the role of sex hormones. Additionally, regional differences in cortical neurogenesis were not addressed. Future research should examine specific cortical areas to better understand the contributions to neurobehavioral outcomes and guide targeted interventions for PPE-induced neurodevelopmental abnormalities. Moreover, although we demonstrated that PPE induces long-term anxiety- and depression-like behaviors in offspring by suppressing RGC function *via* m^{6}A modification, we cannot exclude the possibility that PPE also exerts effects through other mechanisms, such as alterations in growth trajectories. These potential pathways will be explored in subsequent studies.

5. Conclusions

This study reveals the long-term effects of PPE on offspring neurodevelopment, particularly through epigenetic mechanisms involving FTO and m^{6}A modifications, which inhibit RGCs proliferation and differentiation, leading to cortical neurodevelopmental disorders and anxiety- and depression-like behaviors in adulthood. Specifically, PPE enhances FTO nuclear recruitment, reduces m^{6}A modifications of *Crebbp*/*Ep3*00 mRNA, upregulates H3K27ac modifications, and activates genes related to cell cycle and neuronal differentiation, disrupting RGCs development. Notably, exogenous NRG-1 intervention alleviated PPE-induced neurodevelopmental abnormalities and behavioral deficits by promoting RGCs proliferation and improving neuronal and astrocyte structure. These findings provide new molecular insights and intervention strategies for glucocorticoid exposure-related neurodevelopmental disorders during pregnancy, with potential implications for future clinical treatments.

(G) and GFAP (F), (H) staining at PD3 and PD10 with representative images and quantification. Enlarged regions are boxed. Scale bar = 100 μm; enlarged view = 25 μm, $n = 5$. (I) NeuN staining in PW12 offspring with representative images and quantification. Scale bar = 100 μm. (J) mRNA expression levels of *Snap25*, *Dlg4*, and *Shank3* in PW12 offspring, $n = 8$. (K) Transmission Electron Microscopy images of synaptic structures in PW12 offspring. Quantification of PSD thickness, SC width, AZ length, and SV density per field of view (L). Scale bar = 200 nm, $n = 5$. (M) Transmission electron microscopy images of synapses in PW12 offspring within the same field of view with quantification (N). Scale bar = 1 μm, $n = 5$. (O) GFAP staining in PW12 offspring with representative images and Sholl analysis. Scale bar = 50 μm. (P) Quantification of astrocyte percentage, branch length, total branch area, and branch count, $n = 5$. Data are presented as mean ± SEM; ns, no significance; $^*P < 0.05$, $^{**}P < 0.01$ *vs.* Control_S or PPE_N.

Acknowledgments

This work was supported by grants from the National Key Research and Development Program of China (Nos. 2020YFA0803900 and 2024YFA1802700), the National Natural Science Foundation of China (No. 82474017).

Author contributions

Cuiping Qi: conceptualization, writing-original draft, methodology, investigation. Juanjuan Guo: conceptualization, methodology, validation, visualization. Sen Zhu: conceptualization, investigation, software, formal analysis. Keshu Liu: methodology. Yifan Liu: methodology. Mingcui Luo: validation. Xiuping Jin: investigation. Gaole Dai: investigation. Pu Yang: methodology. Shouyi Wang: validation. Xiong Chen: methodology. Huijun Chen: visualization. Hui Wang: supervision, funding acquisition. Dan Xu: writing-review & editing, supervision, project administration, funding acquisition.

Conflicts of interest

The authors declare no competing interests.

Appendix A. Supporting information

Supporting information to this article can be found online at https://doi.org/10.1016/j.apsb.2026.01.026.

References

1. Alrifai N, Puttur A, Ghanem F, Dhital Y, Jabri A, Al-Abdouh A, et al. Maternal and fetal outcomes in those with autoimmune connective tissue disease. *Clin Rheumatol* 2025;**44**:391−401.
2. de Man YA, Dolhain RJ, van de Geijn FE, Willemsen SP, Hazes JM. Disease activity of rheumatoid arthritis during pregnancy: results from a nationwide prospective study. *Arthritis Rheumatol* 2008;**59**:1241−8.
3. Sacchi C, Marino C, Nosarti C, Vieno A, Visentin S, Simonelli A. Association of intrauterine growth restriction and small for gestational age status with childhood cognitive outcomes: a systematic review and meta-analysis. *JAMA Pediatr* 2020;**174**:772−81.
4. Miller SL, Huppi PS, Mallard C. The consequences of fetal growth restriction on brain structure and neurodevelopmental outcome. *J Physiol* 2016;**594**:807−23.
5. Wang T, Chen B, Luo M, Xie L, Lu M, Lu X, et al. Microbiota-indole 3-propionic acid−brain axis mediates abnormal synaptic pruning of hippocampal microglia and susceptibility to ASD in IUGR offspring. *Microbiome* 2023;**11**:245.
6. Ma L, Tian MX, Sun QY, Liu NN, Dong JF, Feng K, et al. Fetal growth restriction mice are more likely to exhibit depression-like behaviors due to stress-induced loss of dopaminergic neurons in the VTA. *FASEB J* 2020;**34**:13257−71.
7. Dash UC, Bhol NK, Swain SK, Samal RR, Nayak PK, Raina V, et al. Oxidative stress and inflammation in the pathogenesis of neurological disorders: mechanisms and implications. *Acta Pharm Sin B* 2025;**15**:15−34.
8. Jamuar SS, Walsh CA. Genomic variants and variations in malformations of cortical development. *Pediatr Clin North Am* 2015;**62**:571−85.
9. Taverna E, Götz M, Huttner WB. The cell biology of neurogenesis: toward an understanding of the development and evolution of the neocortex. *Annu Rev Cell Dev Biol* 2014;**30**:465−502.
10. Tang W, Ma Z, Li B, Yu Z, Zhao X, Yang H, et al. Discovery and proof-of-concept study of a novel highly selective sigma-1 receptor agonist for antipsychotic drug development. *Acta Pharm Sin B* 2025;**15**:5346−65.
11. Farhat LC, Blakey R, Davey Smith G, Fujita A, Shephard E, Stergiakouli E, et al. Networks of neurodevelopmental traits, socio-environmental factors, emotional dysregulation in childhood, and depressive symptoms across development in two U.K. cohorts. *Am J Psychiatry* 2023;**180**:755−65.
12. Doering S, Halldner L, Larsson H, Gillberg C, Kuja-Halkola R, Lichtenstein P, et al. Childhood-onset *versus* adolescent-onset anxiety and depression: epidemiological and neurodevelopmental aspects. *Psychiatry Res* 2022;**312**:114556.
13. Wang Q, Dong X, Lu J, Hu T, Pei G. Constitutive activity of a G protein-coupled receptor, DRD1, contributes to human cerebral organoid formation. *Stem Cell* 2020;**38**:653−65.
14. Chi W, He Y, Chen S, Guo L, Yuan Y, Li R, et al. Advances in research on biomaterials and stem cell/exosome-based strategies in the treatment of traumatic brain injury. *Acta Pharm Sin B* 2025;**15**:3511−44.
15. Jastrzębski MK, Wójcik P, Stępnicki P, Kaczor AA. Effects of small molecules on neurogenesis: neuronal proliferation and differentiation. *Acta Pharm Sin B* 2024;**14**:20−37.
16. Tiberi L, van den Ameele J, Dimidschstein J, Piccirilli J, Gall D, Herpoel A, et al. BCL6 controls neurogenesis through Sirt1-dependent epigenetic repression of selective notch targets. *Nat Neurosci* 2012;**15**:1627−35.
17. Okano H, Temple S. Cell types to order: temporal specification of CNS stem cells. *Curr Opin Neurobiol* 2009;**19**:112−9.
18. Tegowski M, Prater AK, Holley CL, Meyer KD. Single-cell m^6A profiling in the mouse brain uncovers cell type-specific RNA methylomes and age-dependent differential methylation. *Nat Neurosci* 2024;**27**:2512−20.
19. Livneh I, Moshitch-Moshkovitz S, Amariglio N, Rechavi G, Dominissini D. The m^6A epitranscriptome: transcriptome plasticity in brain development and function. *Nat Rev Neurosci* 2020;**21**:36−51.
20. Zhao BS, Wang X, Beadell AV, Lu Z, Shi H, Kuuspalu A, et al. m^6A-dependent maternal mRNA clearance facilitates zebrafish maternal-to-zygotic transition. *Nature* 2017;**542**:475−8.
21. Nguyen TB, Miramontes R, Chillon-Marinas C, Maimon R, Vazquez-Sanchez S, Lau AL, et al. Aberrant splicing in Huntington's disease accompanies disrupted TDP-43 activity and altered m6A RNA modification. *Nat Neurosci* 2025;**28**:280−92.
22. Brouwer J, Hazes JM, Laven JS, Dolhain RJ. Fertility in women with rheumatoid arthritis: influence of disease activity and medication. *Ann Rheum Dis* 2015;**74**:1836−41.
23. Reagan-Shaw S, Nihal M, Ahmad N. Dose translation from animal to human studies revisited. *FASEB J* 2008;**22**:659−61.
24. Nair A, Morsy MA, Jacob S. Dose translation between laboratory animals and human in preclinical and clinical phases of drug development. *Drug Dev Res* 2018;**79**:373−82.
25. Lai X, Zhong L, Fu HX, Dang S, Wang X, Zhang N, et al. Effects of neuregulin-1 on autonomic nervous system remodeling post-myocardial infarction in a rat model. *Neural Regen Res* 2017;**12**:1905−10.
26. Liu M, Chen B, Pei L, Zhang Q, Zou Y, Xiao H, et al. Decreased H3K9ac level of StAR mediated testicular dysplasia induced by prenatal dexamethasone exposure in male offspring rats. *Toxicology* 2018;**408**:1−10.
27. Wang Z, Fan M, Candas D, Zhang TQ, Qin L, Eldridge A, et al. Cyclin B1/Cdk1 coordinates mitochondrial respiration for cell-cycle G2/M progression. *Dev Cell* 2014;**29**:217−32.
28. Tao C, Zhang GW, Huang JJ, Li Z, Tao HW, Zhang LI. The medial preoptic area mediates depressive-like behaviors induced by ovarian hormone withdrawal through distinct GABAergic projections. *Nat Neurosci* 2023;**26**:1529−40.
29. Raffi ER, Marlene P. The etiology of premenstrual dysphoric disorder: 5 interwoven pieces: a better understanding of the causes of PMDD can lead to improved diagnosis and treatment. *Curr Psychiatry* 2017;**16**:20−8.

30. Sit D, Haigh S. Use of "lights" for bipolar depression. *Curr Psychiatry Rep* 2019;**21**:45.
31. Lee HG, Wheeler MA, Quintana FJ. Function and therapeutic value of astrocytes in neurological diseases. *Nat Rev Drug Discov* 2022;**21**: 339−58.
32. Song M, Pebworth MP, Yang X, Abnousi A, Fan C, Wen J, et al. Cell-type-specific 3D epigenomes in the developing human cortex. *Nature* 2020;**587**:644−9.
33. Wang Y, Li Y, Yue M, Wang J, Kumar S, Wechsler-Reya RJ, et al. N^6-Methyladenosine RNA modification regulates embryonic neural stem cell self-renewal through histone modifications. *Nat Neurosci* 2018; **21**:195−206.
34. Yoon KJ, Ringeling FR, Vissers C, Jacob F, Pokrass M, Jimenez-Cyrus D, et al. Temporal control of mammalian cortical neurogenesis by m^6A methylation. *Cell* 2017;**171**. 877-89.e17.
35. Radic T, Frieß L, Vijikumar A, Jungenitz T, Deller T, Schwarzacher SW. Differential postnatal expression of neuronal maturation markers in the dentate gyrus of mice and rats. *Front Neuroanat* 2017;**11**:104.
36. Landry CF, Ivy GO, Brown IR. Developmental expression of glial fibrillary acidic protein mRNA in the rat brain analyzed by *in Situ* hybridization. *J Neurosci Res* 1990;**25**:194−203.
37. Bannister AJ, Kouzarides T. Regulation of chromatin by histone modifications. *Cell Res* 2011;**21**:381−95.
38. Ryu RJ, Easterling TR, Caritis SN, Venkataramanan R, Umans JG, Ahmed MS, et al. Prednisone pharmacokinetics during pregnancy and lactation. *J Clin Pharmacol* 2018;**58**:1223−32.
39. Merkurjev D, Hong WT, Iida K, Oomoto I, Goldie BJ, Yamaguti H, et al. Synaptic N^6-methyladenosine (m^6A) epitranscriptome reveals functional partitioning of localized transcripts. *Nat Neurosci* 2018;**21**: 1004−14.
40. Schmid RS, McGrath B, Berechid BE, Boyles B, Marchionni M, Sestan N, et al. Neuregulin 1-erbB2 signaling is required for the establishment of radial glia and their transformation into astrocytes in cerebral cortex. *Proc Natl Acad Sci U S A* 2003;**100**:4251−6.
41. Reinisch JM, Simon NG, Karow WG, Gandelman R. Prenatal exposure to prednisone in humans and animals retards intrauterine growth. *Science* 1978;**202**:436−8.
42. Benediktsson R, Calder AA, Edwards CR, Seckl JR. Placental 11 beta-hydroxysteroid dehydrogenase: a key regulator of fetal glucocorticoid exposure. *Clin Endocrinol* 1997;**46**:161−6.
43. Burton PJ, Waddell BJ. Dual function of 11β-hydroxysteroid dehydrogenase in placenta: modulating placental glucocorticoid passage and local steroid action. *Biol Reprod* 1999;**60**:234−40.
44. Kobayashi S, Itoh S, Miyashita C, Ait Bamai Y, Yamaguchi T, Masuda H, et al. Impact of prenatal exposure to Mercury and selenium on neurodevelopmental delay in children in the Japan environment and children's study using the ASQ-3 questionnaire: a prospective birth cohort. *Environ Int* 2022;**168**:107448.
45. Johnstone T, van Reekum CM, Urry HL, Kalin NH, Davidson RJ. Failure to regulate: counterproductive recruitment of top-down prefrontal-subcortical circuitry in major depression. *J Neurosci* 2007;**27**: 8877−84.
46. Disner SG, Beevers CG, Haigh EA, Beck AT. Neural mechanisms of the cognitive model of depression. *Nat Rev Neurosci* 2011;**12**:467−77.
47. Kaiser RH, Whitfield-Gabrieli S, Dillon DG, Goer F, Beltzer M, Minkel J, et al. Dynamic resting-state functional connectivity in major depression. *Neuropsychopharmacology* 2016;**41**: 1822−30.
48. Mogg K, Bradley BP. Anxiety and attention to threat: cognitive mechanisms and treatment with attention bias modification. *Behav Res Ther* 2016;**87**:76−108.
49. Schmaal L, Hibar DP, Sämann PG, Hall GB, Baune BT, Jahanshad N, et al. Cortical abnormalities in adults and adolescents with major depression based on brain scans from 20 cohorts worldwide in the ENIGMA major depressive disorder working group. *Mol Psychiatry* 2017;**22**:900−9.
50. Drevets WC, Price JL, Furey ML. Brain structural and functional abnormalities in mood disorders: implications for neurocircuitry models of depression. *Brain Struct Funct* 2008;**213**: 93−118.
51. Shao W, Yang J, He M, Yu XY, Lee CH, Yang Z, et al. Centrosome anchoring regulates progenitor properties and cortical formation. *Nature* 2020;**580**:106−12.
52. Kriegstein A, Alvarez-Buylla A. The glial nature of embryonic and adult neural stem cells. *Annu Rev Neurosci* 2009;**32**:149−84.
53. Li L, Zang L, Zhang F, Chen J, Shen H, Shu L, et al. Fat mass and obesity-associated (FTO) protein regulates adult neurogenesis. *Hum Mol Genet* 2017;**26**:2398−411.
54. Weng YL, Wang X, An R, Cassin J, Vissers C, Liu Y, et al. Epitranscriptomic m^6A regulation of axon regeneration in the adult mammalian nervous system. *Neuron* 2018;**97**. 313-25.e6.
55. Yen YP, Chen JA. The m^6A epitranscriptome on neural development and degeneration. *J Biomed Sci* 2021;**28**:40.
56. Mendel M, Delaney K, Pandey RR, Chen KM, Wenda JM, Vågbø CB, et al. Splice site m^6A methylation prevents binding of U2AF35 to inhibit RNA splicing. *Cell* 2021;**184**. 3125-42.e25.
57. Xiao W, Adhikari S, Dahal U, Chen YS, Hao YJ, Sun BF, et al. Nuclear m^6A reader YTHDC1 regulates mRNA splicing. *Mol Cell* 2016;**61**:507−19.
58. Cheng FW, Peng LM, Luo D. Methyltransferase-like 3 promotes the progression of lung cancer *via* activating PI3K/AKT/mTOR pathway. *Clin Exp Pharmacol Physiol* 2022;**49**:748−58.
59. Liu J, Yue Y, Han D, Wang X, Fu Y, Zhang L, et al. A METTL3−METTL14 complex mediates mammalian nuclear RNA N^6-adenosine methylation. *Nat Chem Biol* 2014;**10**:93−5.
60. Chang X, Lu K, Wang L, Lv M, Fu W. Astraglaus polysaccharide protects diabetic cardiomyopathy by activating NRG1/ErbB pathway. *Biosci Trends* 2018;**12**:149−56.
61. Sun Y, Ikrar T, Davis MF, Gong N, Zheng X, Luo ZD, et al. Neuregulin-1/ErbB4 signaling regulates visual cortical plasticity. *Neuron* 2016;**92**:160−73.
62. Liu J, Kern JA. Neuregulin-1 activates the JAK−STAT pathway and regulates lung epithelial cell proliferation. *Am J Respir Cell Mol Biol* 2002;**27**:306−13.
63. Odintsov I, Mattar MS, Lui AJW, Offin M, Kurzatkowski C, Delasos L, et al. Novel preclinical patient-derived lung cancer models reveal inhibition of HER3 and MTOR signaling as therapeutic strategies for NRG1 fusion-positive cancers. *J Thorac Oncol* 2021;**16**: 1149−65.